processes

MDPI

*Article*

# Optimization and Efficiency of Novel Magnetic-Resin-Based Approaches for Enhanced Nickel Removal from Water

**Marija Maletin [1], Jasmina Nikić [1,*], Vesna Gvoić [2], Jovana Pešić [1], Željka Cvejić [1], Aleksandra Tubić [1] and Jasmina Agbaba [1]**

[1] Department of Chemistry, Biochemistry and Environmental Protection, Faculty of Sciences, University of Novi Sad, Trg Dositeja Obradovića 3, 21000 Novi Sad, Serbia; marijac@dh.uns.ac.rs (M.M.); jovana.pesic@dh.uns.ac.rs (J.P.); zeljka.cvejic@df.uns.ac.rs (Ž.C.); aleksandra.tubic@dh.uns.ac.rs (A.T.); jasmina.agbaba@dh.uns.ac.rs (J.A.)

[2] Faculty of Technical Sciences, Department of Graphic Engineering and Design, University of Novi Sad, Trg Dositeja Obradovića 6, 21000 Novi Sad, Serbia; kecic@uns.ac.rs

* Correspondence: jasmina.nikic@dh.uns.ac.rs

**Abstract:** Nickel contamination in water is a critical issue due to its toxicity and persistence. This study presents a novel magnetic resin, developed by modifying Lewatit® MonoPlus TP 207 with magnetite nanoparticles, to enhance adsorption capacity and facilitate efficient separation. A Definitive Screening Design (DSD) was employed to identify and optimize key parameters affecting nickel adsorption, including pH, resin dosage, initial nickel concentration, and the presence of competing ions (calcium and magnesium). The DSD analysis revealed that pH and magnesium concentration were the most significant factors influencing nickel removal. Optimal conditions were determined as pH 7, 270 min contact time, resin dosage of 0.5 mL/L, initial nickel concentration of 110 µg/L, calcium concentration of 275 mg/L, and magnesium concentration of 52.5 mg/L, achieving a maximum removal efficiency of 99.21%. The magnetic resin exhibited enhanced adsorption capacity and faster kinetics compared to the unmodified resin, leading to more efficient nickel removal. Moreover, its magnetic properties facilitated rapid separation from treated water, offering practical advantages for real-world applications. This study demonstrates the effective use of DSD in optimizing adsorption parameters and underscores the potential of magnetic resin as a sustainable and efficient adsorbent for water treatment.

**Keywords:** nickel removal; aqueous solution; magnetic resin; adsorption; process optimization; definitive screening design; ion exchange resin

check for updates

**Citation:** Maletin, M.; Nikić, J.; Gvoić, V.; Pešić, J.; Cvejić, Ž.; Tubić, A.; Agbaba, J. Optimization and Efficiency of Novel Magnetic-Resin-Based Approaches for Enhanced Nickel Removal from Water. *Processes* **2024**, *12*, 2287. https://doi.org/10.3390/pr12102287

Academic Editor: Anna Wołowicz

Received: 24 September 2024
Revised: 9 October 2024
Accepted: 14 October 2024
Published: 18 October 2024

**Copyright:** © 2024 by the authors. Licensee MDPI, Basel, Switzerland. This article is an open access article distributed under the terms and conditions of the Creative Commons Attribution (CC BY) license (https://creativecommons.org/licenses/by/4.0/).

## 1. Introduction

Water contamination from both natural processes and human activities has become a major global concern in recent years [1,2]. Among the various pollutants, metals are particularly troubling due to their persistence, non-biodegradability, and toxicity, making them some of the most hazardous contaminants in water [3,4]. Nickel, often found alongside antimony, arsenic, and sulfur, is notable for its high thermal and electrical conductivity [5]. However, excessive exposure to nickel has been linked to a range of serious health issues, including neurotoxicity, hepatotoxicity, nephrotoxicity, gastrointestinal disorders, dermatitis, and severe lung damage. Long-term exposure to nickel in drinking water has also been associated with genetic alterations and an increased risk of cancer [6–8]. The International Agency for Research on Cancer (IARC) classifies inhaled nickel compounds as carcinogenic (Group 1) and metallic nickel as a possible human carcinogen (Group 2B) [9]. To mitigate the health risks associated with nickel, the European Parliament's Directive (EU) 2020/2184 recommends a maximum allowable concentration (MAC) of 20 µg/L in drinking water [10–12].

Nanotechnology is emerging as a key innovation in water treatment, with various nanomaterials demonstrating exceptional capacities for heavy metal adsorption [13–16]. Despite their benefits, effectively recovering nanoparticles such as metal oxides, carbon-based materials, layered double hydroxides, and nano-polymer composites from purified water remains challenging [17,18]. Traditional separation methods like filtration and sedimentation are often inefficient, with high operational costs and energy demands. In contrast, magnetic separation offers an effective alternative by utilizing the magnetic properties of iron-based nanoparticles for rapid and efficient recovery. This green approach not only enhances separation efficiency but also reduces energy consumption and operational costs, making it favorable for sustainable water treatment [19,20].

Among magnetic nanomaterials, iron oxide nanoparticles like magnetite ($Fe_3O_4$) and maghemite ($\gamma$-$Fe_2O_3$) have been widely explored for heavy metal removal due to their magnetic properties and ease of synthesis [21–23]. However, magnetic nanoparticles can aggregate in solution, reducing their effectiveness in fixed-bed or continuous-flow systems. To overcome this limitation, stabilizing magnetic nanoparticles with support media such as carbon-based materials, polymers, biopolymers, and organic substances has emerged as a promising strategy, leading to the development of magnetic nanocomposite materials with enhanced characteristics [24–26].

Ion exchange resins are a particularly promising support material for stabilizing magnetic nanoparticles due to their mechanical strength and chemical stability. By combining the advantages of nanoparticles and ion exchange resins, resin-based nanocomposites offer high efficiency for metal adsorption [27–30]. While traditional strongly and weakly acidic ion exchange resins can be effective for metal removal, they often exhibit low selectivity [31–35]. In contrast, chelating ion exchange resins possess covalently bonded side chains with donor atoms, enabling them to form coordination bonds with heavy metal ions, thereby increasing their affinity for specific metals [36,37]. For instance, the iminodiacetate functional group in the commercial chelating resin Lewatit® MonoPlus TP 207 effectively binds divalent metal ions like Ni(II) through chelation, enhancing both selectivity and efficiency [38]. Additionally, the mechanical stability and high specificity of Lewatit® MonoPlus TP 207 for metal ions make it an ideal candidate for modification with magnetic nanoparticles, enabling the development of novel magnetic polymer-based adsorbents for nickel removal. These magnetic polymer-based adsorbents represent an emerging class of hybrid organic–inorganic materials, offering distinct advantages over traditional adsorbents and enhancing adsorption capacity for metal ions. Unlike activated carbon or non-magnetic polymer resins, their magnetic properties allow for rapid and efficient separation from treated water, reducing both time and costs associated with post-treatment recovery. Furthermore, compared to silica-based materials or bioadsorbents, magnetic-resin-based adsorbents demonstrate superior mechanical stability, chemical resistance, and reusability, making them suitable for repeated use in continuous processes under diverse environmental conditions [26,39,40].

Various factors, such as pH, nickel concentration, ionic strength, the presence of other competing ions, and organic matter, influence the efficiency of nickel adsorption or removal processes. Aranda-García et al. [41] found that higher ionic strength can reduce adsorption efficiency, which is particularly pronounced when divalent cations like $Ca^{2+}$ and $Mg^{2+}$ are present, as they compete with nickel ions for adsorption sites, further diminishing the adsorption capacity [42]. Another study emphasizes that pH is a critical factor in nickel adsorption, as it affects the precipitation and adsorption processes, which could be extrapolated to the behavior of nickel ions under different pH conditions [43]. Given the complexity of these factors, optimizing the treatment process requires a careful experimental design. Traditional methods, such as Response Surface Methodology (RSM), require a large number of experimental runs and are most effective once the primary factors influencing the process have been identified [44–50]. The Definitive Screening Design (DSD), in contrast, uses a numerical algorithm to maximize the determinant of the main effects model matrix, effectively identifying significant factors, predicting two-factor interactions, and estimating

model coefficients across the entire experiment with fewer runs [51–54]. DSD is particularly advantageous for the initial screening and optimization of multiple factors with fewer runs, whereas RSM is better suited for detailed optimization once key factors have been established [55–58].

In this study, the DSD was employed to enhance efficiency and optimize key parameters influencing nickel removal from water using a novel magnetic resin. This resin was synthesized by incorporating magnetite nanoparticles into the commercially available Lewatit® MonoPlus TP 207, which contains iminodiacetate functional groups. Both unmodified and magnetic resins underwent comprehensive characterization, including BET surface area analysis, SEM/EDS imaging, FTIR spectroscopy, XRD analysis, and Raman spectroscopy. To optimize experimental conditions and evaluate the impact of key operational parameters—such as initial nickel concentration, resin dosage, and magnesium and calcium concentrations, as well as pH—on nickel removal efficiency, experiments were conducted over a pH range of 6.0–8.4 with DSD applied. Additionally, kinetic and isotherm studies were performed at neutral pH (around 7.0 ± 0.2), supported by mathematical models, to elucidate the mechanism of nickel removal by the magnetic resin.

## 2. Materials and Methods

### 2.1. Reagents

Stock solutions of Ni(II) (100 mg/L) were diluted in deionized water to the desired metal concentrations. $FeSO_4 \cdot 7H_2O$ and $FeCl_3 \cdot 6H_2O$ (Lach:ner, Czech Republic), were used for preparation of the magnetic resin. $MgCl_2 \cdot 6H_2O$ (Sigma Aldrich, USA), $CaCO_3$ (Sigma Aldrich, USA), were employed to create specific synthetic matrices with various calcium and magnesium ion concentrations according to the experimental design. NaOH, $HNO_3$ (Sigma Aldrich, USA) were used during the resin activation, as well as for adjusting the pH of the solution. The deionized water used in the work was produced in the laboratory using a LABCONCO treatment system (WaterPro RO/PS Station, USA).

### 2.2. Materials

Commercial macroporous cation exchange resin, Lewatit® MonoPlus TP 207 (Bayer, Berlin, Germany) with iminodiacetate group (-N $(CH_2COOH)_2$) (Table 1) was used for the synthesis of magnetic resin as well for comparison of nickel removal performance. Before adsorption experiments, dry resin was activated with 4% NaOH solution by continuously passing the solution through a column filled with 100 mL of resin, at a flow rate of 20 mL/min. Afterwards, the resin was rinsed several times with deionized water until the pH was neutral and stored before use.

**Table 1.** Characteristics of the Lewatit® MonoPlus TP 207 resin applied for Ni(II) removal.

| Resin Type | Chelating Resin |
|---|---|
| Matrix | Polystyrene |
| Structure | Macroporous |
| Functional group | Iminodiactetic |
| Uniformity coefficient | 1.1 |
| Mean bead size (mm) | 0.61 ± 0.05 |
| Water retention (%) | 55–60 |
| Capacity (eq/L) | 2.0 |

### 2.3. Synthesis of Magnetic Resin

The modification of Lewatit® MonoPlus TP 207 with magnetite nanoparticles was conducted in a single-step process using an adapted coprecipitation method, as described in the study by Sikora et al. [27]. Initially, $FeSO_4 \cdot 7H_2O$ (11.45 g) and $FeCl_3 \cdot 6H_2O$ (20.21 g) were dissolved separately in 50 mL of distilled water and then combined, followed by stirring for 30 min. Afterward, 25 g of dry Lewatit® MonoPlus TP 207 resin was added to the iron solution and stirred continuously for 2 h at room temperature. The impregnated

resin was then washed with distilled water to remove excess iron particles. Subsequently, to synthesize the magnetite nanoparticles and regenerate the resin, 0.2 M NaOH was added to the mixture, which was stirred for 1 h. The synthesized magnetic resin was separated using an external magnet, washed thoroughly with distilled water until neutral pH was achieved, and dried at 105 °C

### 2.4. Resins Characterization

The morphological characteristics of both resins, modified and unmodified, were analyzed using a scanning electron microscope (SEM), while the qualitative and semiquantitative elemental composition of the surface of the resins was examined by energy-dispersive spectroscopy (EDS) (Hitachi TM3030, Tokyo, Japan). The FTIR spectra of the resins were recorded on a spectrophotometer at a range of 400–4000 $cm^{-1}$ (FTIR Nexus 670, Thermonicolet, USA). Raman spectra were obtained with Thermo Scientific DXR Raman Microscope coupled with a 532 nm wavelength laser, with the power level set to 9 mW. Specimens were illuminated for 10 s in 10 repetitions at room temperature. X-ray diffraction (XRD) patterns were obtained with the Rigaku MiniFlex 600 (Tokyo, Japan) diffractometer using Cu-Kα radiation in the range from 10° to 90°, with a step of 0.02° and dwell time of 3 s. The identification of compounds from the resulting diffractograms was carried out using the Pcpdfwin database, version 2.4 JCPDS-ICDD. To measure the magnetic susceptibility of resin samples, the MS2B device manufactured in Bartington, UK, was used. The MS2B sensors are used for the measurement of magnetic susceptibility of soil, rock and sediment samples and operate on the principle of comparison between the magnetic permeability of air and the relative permeability obtained with the contribution of the sample magnetic permeability. The sensors are calibrated to the diamagnetism of water, where the mass susceptibility is $-0.72 \times 10^{-5}$ SI.

### 2.5. Adsorption Experiments

The batch experiments were carried out in a series of 800 mL glass beakers containing 500 mL Ni(II) aqueous solution. In the kinetic experiments, the resin dose was 0.5 mL/L, and the three different initial concentrations of nickel (0.05 mg/L, 0.5 mg/L and 1 mg/L) were investigated over a period of 24 h. The initial pH of the solutions was adjusted to 7.0 ± 0.2 by addition of 0.1 M $HNO_3$ and/or NaOH. The suspensions were stirred (120 rpm, 22 °C) at predetermined time intervals (0.5, 1, 2, 3, 4, 5, 6, 7, 8, 12, 24 h) on a mechanical stirrer. Afterwards, the supernatants were separated from the magnetic resin using an external magnet or decanted in the case of the unmodified resin. Residual nickel and iron concentrations in the supernatant were analyzed by inductively coupled plasma mass spectrometry (ICP-MS). Adsorption isotherms were obtained in a similar manner by varying the initial nickel concentration (0.05–20 mg/L) while maintaining the same conditions as those used in the kinetic experiments.

Adsorption capacity of resins for Ni(II) was calculated based on the difference between the initial and equilibrium concentrations of nickel in the solution, according to Equation (1).

$$q_e = (C_0 - C_e) \times V/m \quad (1)$$

where $q_e$ is the adsorption capacity (mg/g), $C_0$ is the initial concentration of nickel (mg/L), $C_e$ is the equilibrium concentration of nickel (mg/L), V is the volume of the solution (L), and m is the mass of the resin used (g). This calculation allowed us to determine the amount of nickel adsorbed per gram of resin under the given experimental conditions.

The percentage removal of nickel was calculated using Equation (2):

$$\% \text{ Removal} = (C_0 - C_e)/C_0 \times 100 \quad (2)$$

This equation quantifies the efficiency of nickel ion removal as a percentage of the initial concentration. These calculations provided an insight into the adsorption capacity of the resin and the effectiveness of nickel removal under varying experimental conditions.

#### 2.5.1. Adsorption Kinetics

To assess the rate at which the adsorbate is taken up and to explore potential mechanisms or pathways involved in the adsorption of nickel on the both resins, three kinetic models were applied: the Lagergren pseudo-first-order model, the pseudo-second-order model, and the Elovich model. The nonlinear equations and the parameters for these kinetic models are outlined in Table S1.

#### 2.5.2. Adsorption Isotherms

In order to evaluate the maximum adsorption capacity of the resins and to gain an enhanced understanding of the adsorption mechanisms, the equilibrium data were analyzed using the two most common isotherm models, Freundlich and Langmuir models. Table S1 details the nonlinear mathematical equations, associated parameters, and key assumptions underlying these isotherm models.

### *2.6. Definitive Screening Design*

DSD was applied as an effective, complete and flexible novel statistical approach, giving the opportunity to narrow down the long list of significant variables and interactions to only a few significant effects. The experiments were small and efficient, involving several variables [56,57]. This study was designed to include six continuous factors: pH, contact time, resin dosage, nickel, calcium and magnesium concentration. Specific levels for each factor (Table 2) were selected based on data from related research [59,60]. The software JMP 13 (version 13, SAS Institute, North Carolina, USA) was used for the design of the experiment and statistical data processing. Experimental data were modeled using stepwise regression analysis, which included the main factors and their interactions, with statistical significance considered for $p$ values $\leq 0.05$.

**Table 2.** Process parameters with experimental levels.

| Factor | Unit | Coded Value | Level | | |
|---|---|---|---|---|---|
| | | | Low (−1) | Central (0) | High (+1) |
| pH | - | $X_1$ | 5 | 7 | 9 |
| Contact time | min | $X_2$ | 30 | 255 | 480 |
| Resin dosage | mL/L | $X_3$ | 0.5 | 2.75 | 5 |
| Ni concentration | µg/L | $X_4$ | 20 | 110 | 200 |
| Ca concentration | mg/L | $X_5$ | 50 | 275 | 500 |
| Mg concentration | mg/L | $X_6$ | 5 | 52.5 | 100 |

### *2.7. Analytical Methods*

pH measurements were carried out using an InoLab pH/ION 735 instrument (UK). Nickel concentrations in water samples were determined using the ICP-MS technique (Agilent Technologies 7700 Series ICP-MS, Tokyo, Japan). Method detection limits for the nickel were 0.001 mg/L.

## 3. Results and Discussion

### *3.1. Resin Characterization*

The SEM analysis confirmed the spherical morphology of both the unmodified and magnetic resin beads (Figure 1a,b). At higher magnification, the surfaces of both materials appeared rough and highly porous (Figure 1c,d). The diameter of the resin beads was measured to be between 400 and 450 µm, demonstrating that the incorporation of magnetite nanoparticles did not significantly affect the overall particle size (Figure 1). This finding is consistent with the spherical morphology observed in the SEM images.

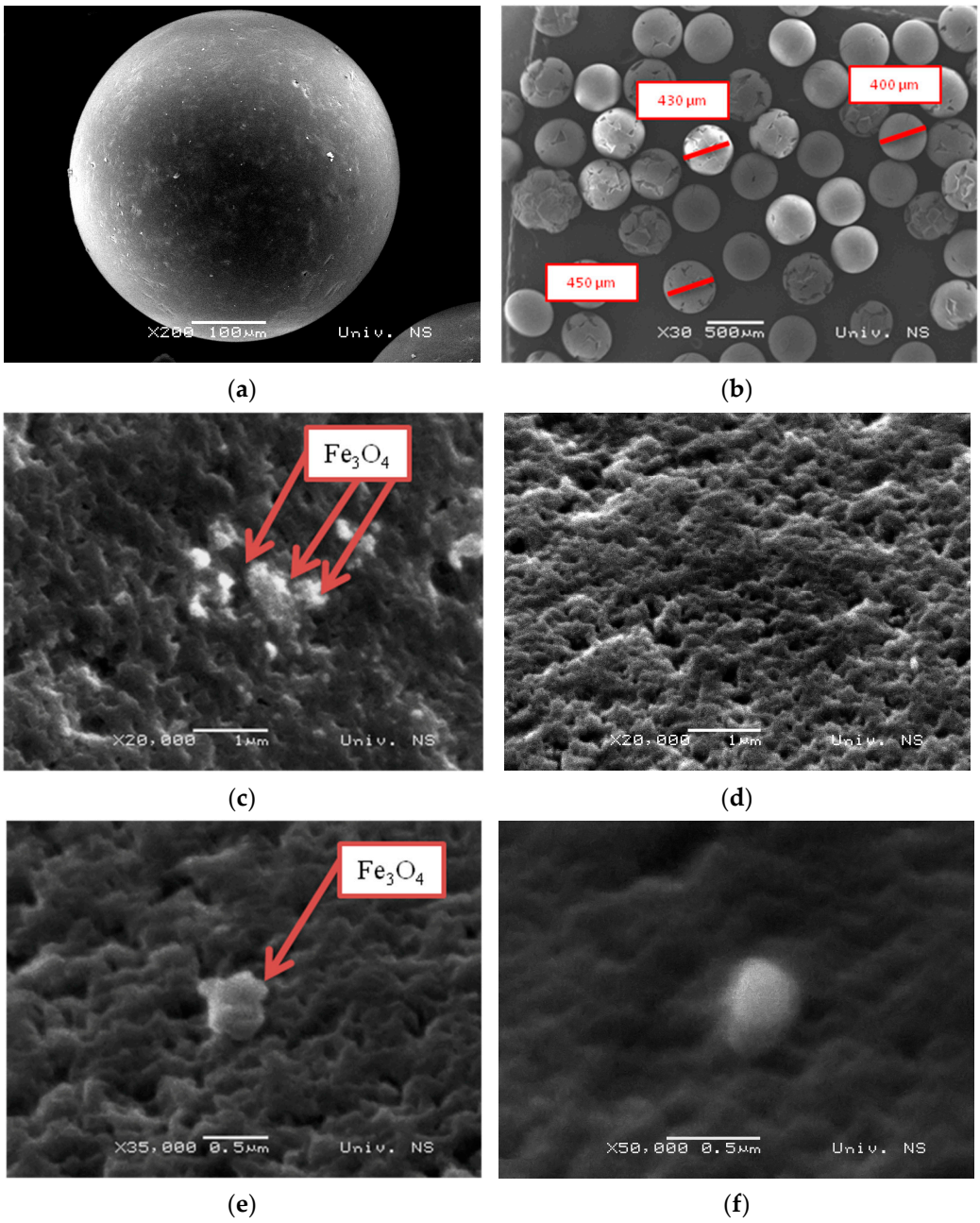


**Figure 1.** SEM images of (**a**,**b**) Lewatit® MonoPlus TP 207, (**c**–**f**) magnetic resin.

Notably, while the SEM images of both unmodified and magnetic resins showed no significant differences in overall morphology, the primary magnetite nanoparticles were visible as irregular hexagonal crystals on the surface of the magnetic resin (Figure 1e,f). This confirms the successful incorporation of magnetite without altering the resin's surface structure. Post-adsorption SEM analysis, conducted after Ni(II) uptake, revealed no observable differences in the surface structure, indicating that the adsorption process did not significantly alter the resin morphology.

The elemental analysis, obtained through EDS measurements for both the unmodified and modified resins, is shown in Figure 2. The elemental composition analysis of Lewatit® MonoPlus TP 207 revealed that carbon (75.57 Wt%) is the most abundant surface element, as expected, given that it forms the main component of the polymer matrix. Oxygen (14.19 Wt%) is the second most prevalent element, consistent with its role in both the resin's

structure and the iminodiacetate functional group. Additionally, sodium (10.24 Wt%) is detected as part of the activated iminodiacetate group in the commercial resin (Figure 2a).

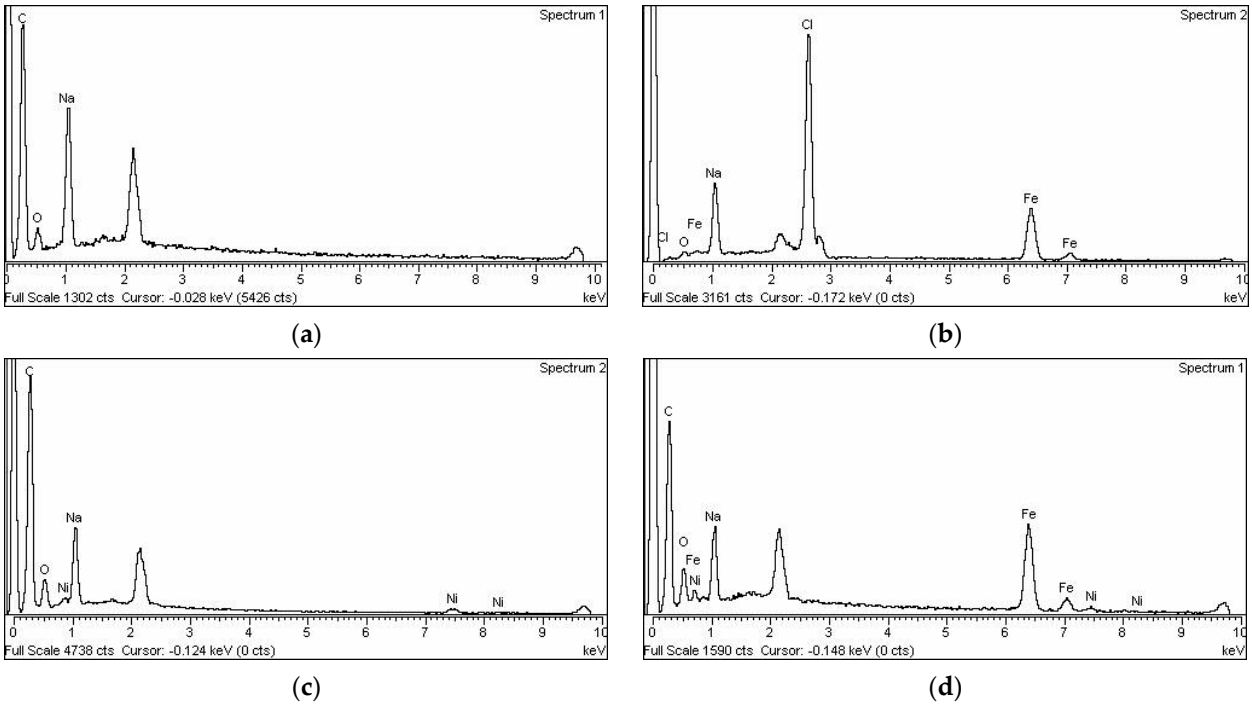


**Figure 2.** EDS analysis of (**a**) Lewatit® MonoPlus TP 207 before Ni(II) adsorption; (**b**) magnetic resin before Ni(II) adsorption; (**c**) Lewatit® MonoPlus TP 207 after Ni(II) adsorption; and (**d**) magnetic resin after Ni(II) adsorption.

Upon modification to produce the magnetic resin, changes in the surface composition were observed: carbon remains the dominant element (54.17 Wt%), while oxygen content increased to 18.41 Wt%, and sodium content decreased to 7.43 Wt%. Importantly, iron was detected at 19.99 Wt%, indicating the successful integration of $Fe_3O_4$ nanoparticles into the resin structure (Figure 2b).

Following metal adsorption using the commercial resin, a reduction in sodium content was noted, alongside the appearance of characteristic peaks for adsorbed nickel, suggesting that the adsorption of heavy metals primarily occurs through an ion-exchange mechanism (Figure 2c). For the magnetic resin, nickel adsorption did not lead to a significant decrease in either iron or sodium content, implying a combined mechanism of ion exchange and sorption (Figure 2d). This hybrid adsorption process enhances the magnetic resin's capacity for nickel removal compared to the commercial resin by combining the mechanisms of ion exchange and sorption [27]. The magnetic modification not only retains the ion-exchange functionality of the original resin but also introduces additional sorption sites provided by the $Fe_3O_4$ nanoparticles. This dual mechanism improves adsorption efficiency, resulting in faster kinetics and higher adsorption capacity for nickel ions from aqueous solutions.

The phase and crystalline structures of Lewatit® MonoPlus TP 207 and the magnetic resin were analyzed using X-ray powder diffraction (XRD), with the corresponding patterns shown in Figure 3.

The XRD pattern of the commercial resin contains broad and low-intensity peaks, indicating that the resin is predominantly amorphous with a low degree of crystallinity. Previous research has also demonstrated that unmodified resins exhibit wide diffraction peaks within the range of 10° to 80°, with prominent peaks appearing between 20° and 50° (specifically at $2\theta$ = 23°, 29°, 39° and 47 in this study). These peaks correspond to the scattering behavior of the cross-linked polymer network and reflect its amorphous characteristics [61,62].

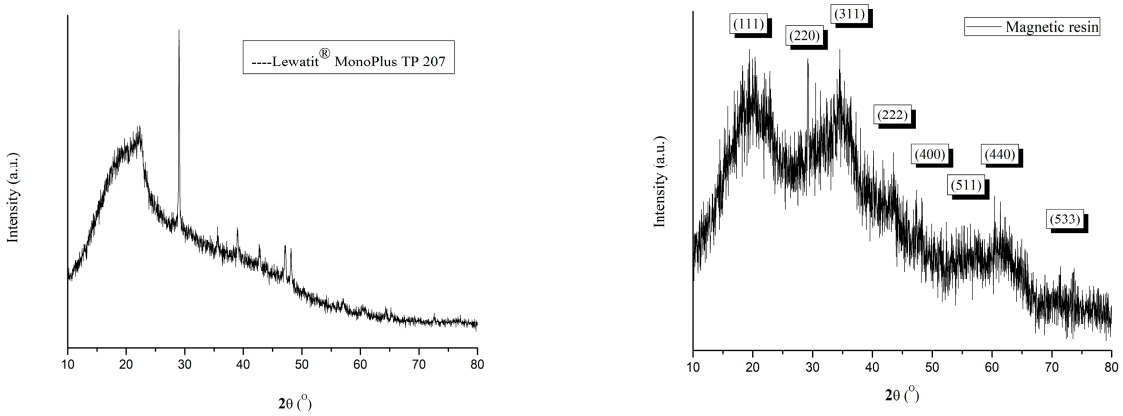


(**a**) (**b**)

**Figure 3.** XRD pattern of (**a**) Lewatit® MonoPlus TP 207 before Ni(II) adsorption; (**b**) magnetic resin before Ni(II) adsorption.

The XRD peaks for the magnetic resin are broad and exhibit low intensity, indicating that the resin is predominantly amorphous with a minor degree of crystallinity. However, eight sharper diffraction peaks were observed at 2θ angles of 19°, 30°, 35°, 43°, 50°, 57°, 63°, and 74° (Figure 3) on the XRD spectrum of the magnetic resin. These peaks correspond to the (111), (220), (311), (222), (400), (511), (440), and (533) crystallographic planes of the magnetite ($Fe_3O_4$) phase, as identified by the JCPDS card number 11-0614 for magnetite [27,63]. These XRD patterns confirm the successful synthesis of magnetite nanoparticles via a green synthesis method.

As shown in Figure 4, FTIR analysis was conducted to investigate the chemical composition of both the unmodified ion exchange resin (Lewatit® MonoPlus TP 207) and the modified magnetic resin. The FTIR spectra of both materials exhibited peaks within the wavenumber range of 500–4500 $cm^{-1}$. The most intense peak, at 3440 $cm^{-1}$, corresponds to N-H and O-H stretching vibrations, which are indicative of hydrogen bonding within the iminodiacetate functional group. Several peaks specific to the polystyrene structure were observed within the range of 2800–3060 $cm^{-1}$, with a prominent peak at 2922 $cm^{-1}$, indicative of C-H stretching vibration from the aliphatic chains of the resin matrix, particularly the methylene ($-CH_2$) and methyl ($-CH_3$) groups. The peak at 1626 $cm^{-1}$ is attributed to N-H bending and C-N stretching vibrations, indicating the amine functionality within the resin structure, while C-O stretching vibrations appear at 1404 $cm^{-1}$, associated with the carboxylate and ester functional groups. Additionally, deformation vibrations of the aromatic rings within the polystyrene backbone of the resin matrix are noted around 1098 and 906 $cm^{-1}$ (Figure 4).

After the sorption of Ni(II) ions, notable changes are observed in the FTIR spectrum of Lewatit® MonoPlus TP 207, providing an insight into the binding mechanisms and interactions between the resin's functional groups and the metal ions (Figure 4a). One of the key changes observed is the reduction in the intensity of the peak around 3440 $cm^{-1}$. This peak corresponds to N-H and O-H stretching vibrations, and its decrease suggests active involvement of the iminodiacetate groups, particularly the amine and hydroxyl moieties, in the adsorption process. The reduction in peak intensity indicates the participation of these groups in binding Ni(II) ions, likely through coordination or chelation, confirming their role as primary active sites for metal ion complexation.

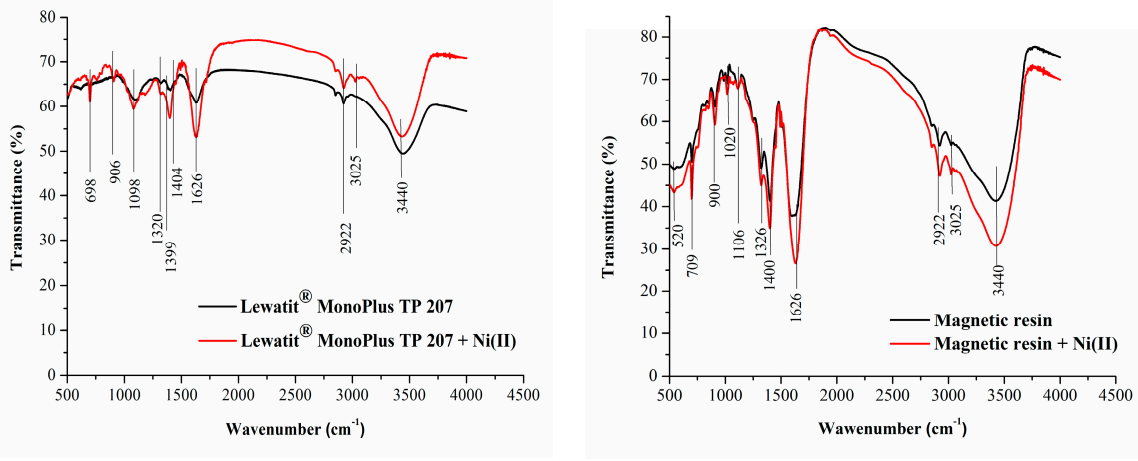


**Figure 4.** FTIR spectrum of (**a**) Lewatit® MonoPlus TP 207 before and after sorption of Ni(II); (**b**) the magnetic resin before and after sorption of Ni(II).

Another important observation is the emergence of a new band around 698 $cm^{-1}$, which is attributed to M–O vibrations (where M denotes the metal, in this case, Ni). This peak signifies the formation of metal–oxygen bonds, indicating that the carboxylate oxygen atoms from the iminodiacetate functional groups participate in the binding of Ni(II) ions. The presence of this peak suggests that the adsorption of Ni(II) onto the resin involves a chelation mechanism, where the metal ions coordinate with the oxygen atoms in the carboxyl groups of the iminodiacetate. This band is a clear indicator of the metal–ligand interaction and confirms the successful adsorption of Ni(II) ions onto the resin. Additionally, changes in the intensity of peaks around 1626 $cm^{-1}$ and 1404 $cm^{-1}$ are observed after Ni(II) adsorption. The peak at 1626 $cm^{-1}$ is associated with C=O stretching vibrations of the carboxylate group and N-H bending, while the peak at 1404 $cm^{-1}$ corresponds to the C-O stretching of the carboxylate group. After adsorption, the intensity and sometimes slight shifts of these peaks suggest changes in the electronic environment of these functional groups, as they interact with Ni(II) ions. The reduction or alteration in peak intensity implies that the carboxylate groups are directly involved in the coordination with Ni(II), supporting the idea that ion exchange and chelation are the main mechanisms for metal binding. Peaks at 2922 $cm^{-1}$, related to C-H stretching vibrations from aliphatic methylene and methyl groups, also exhibit changes in intensity. While these groups are not directly involved in metal ion binding, the changes in their peaks might be attributed to conformational adjustments in the resin matrix as a result of the sorption process. This suggests that the resin undergoes some structural adjustments upon Ni(II) binding, possibly optimizing the spatial arrangement of functional groups to facilitate coordination.

Moreover, after Ni(II) adsorption, the overall transmittance of the FTIR peaks is generally higher in the Ni(II)-loaded resin compared to the unsorbed resin, which could indicate that some functional groups have formed stronger complexes with Ni(II), reducing their vibrational freedom. The higher transmittance values in certain bands imply that the adsorption process stabilizes certain functional groups, locking them into a more rigid structure as they participate in binding. Overall, the FTIR spectral changes after Ni(II) adsorption highlight the active role of iminodiacetate functional groups in the sorption process. The observed reduction in peak intensity around 3440 $cm^{-1}$, the new band at 698 $cm^{-1}$ indicating M–O bond formation, and changes in carboxylate-associated peaks collectively confirm that the carboxyl and amine groups within the resin actively coordinate and chelate Ni(II) ions. These interactions not only demonstrate the efficiency of Lewatit® MonoPlus TP 207 in removing Ni(II) from solution but also provide an insight into the binding mechanisms, predominantly involving ion exchange and chelation facilitated by iminodiacetate functional groups.

The FTIR spectrum of the magnetic resin closely resembles that of Lewatit® MonoPlus TP 207, with a few distinct differences due to the magnetic modification. Specifically, the spectrum shows high-intensity peaks at 3440 $cm^{-1}$ and 1320 $cm^{-1}$, which can be attributed to the stretching vibrations of the -$CH_3$ and C=C groups, respectively. Most notably, the peak at 520 $cm^{-1}$ corresponds to Fe-O stretching vibrations at tetrahedral and octahedral sites, confirming the successful incorporation of magnetite ($Fe_3O_4$) into the resin structure (Figure 4b).

Before Ni(II) adsorption, the magnetic resin exhibits typical FTIR features of both the organic polymer matrix and the magnetic component. The peak around 3440 $cm^{-1}$ corresponds to N-H and O-H stretching vibrations, similar to the non-magnetic resin, indicating the presence of iminodiacetate functional groups. The Fe-O stretching vibration at 520 $cm^{-1}$ is a clear signature of the magnetite nanoparticles, suggesting that they are effectively embedded within the resin structure and are available for interaction during the adsorption process. After Ni(II) adsorption, the FTIR spectra of the magnetic resin show largely similar features to the pre-adsorption state, with some notable changes in the intensity of specific bands. Key changes are observed at 520 $cm^{-1}$, 709 $cm^{-1}$, 1400 $cm^{-1}$, 1626 $cm^{-1}$, 2922 $cm^{-1}$, and 3440 $cm^{-1}$, indicating that both the organic matrix and the magnetite component participate in the sorption process.

An increased intensity of the peak at 3440 $cm^{-1}$ after Ni(II) adsorption suggests that the N-H and O-H groups in the iminodiacetate functional moieties play an active role in binding Ni(II) ions. Unlike in the non-magnetic resin, where the peak's intensity decreases, the increased intensity here may indicate the synergistic effect between the iminodiacetate groups and the magnetite nanoparticles, enhancing the sorption capacity and providing additional binding sites for Ni(II). This interaction likely reduces the competition between the resin's functional groups and the metal ions, allowing for more efficient binding. Additionally, the increase in intensity of the peak at 1626 $cm^{-1}$, which corresponds to C=O stretching and N-H bending vibrations, further supports the active participation of the carboxylate groups in Ni(II) binding. A similar change is observed for the peak at 1400 $cm^{-1}$, associated with C-O stretching, suggesting that both amine and carboxylate functionalities contribute to the sorption process by forming coordination complexes with Ni(II). These increased intensities reflect a higher degree of metal–ligand interaction facilitated by the resin's modified structure.

The enhanced peak at 520 $cm^{-1}$ after Ni(II) sorption is particularly significant as it corresponds to Fe-O vibrations. This indicates that the magnetite phase itself is actively involved in the sorption process. The magnetite nanoparticles provide additional binding sites through a surface adsorption mechanism or act as a co-adsorbent, promoting a dual mechanism of metal binding. The presence of this strong Fe-O peak not only confirms that magnetite is retained within the resin matrix after sorption but also emphasizes its role in enhancing the overall adsorption capacity [27,63–65]. Additionally, the appearance and increased intensity of the band at 709 $cm^{-1}$ also hint at further interactions between Ni(II) and the resin, possibly involving metal–oxygen coordination or additional binding facilitated by the resin's modified surface.

In summary, the FTIR spectra after Ni(II) sorption indicate that the magnetic resin retains the characteristics of the original polymer while actively incorporating the magnetite phase. Both the iminodiacetate functional groups and magnetite nanoparticles contribute to Ni(II) adsorption. The presence of magnetite enhances the resin's performance by providing additional sorption sites and supporting both ion exchange and surface adsorption mechanisms, thereby improving sorption efficiency and kinetics.

The collected Raman spectra for all samples confirm the highly amorphous structure of the resin (Figure 5). The decrease in Raman peak intensity after Ni(II) adsorption can be attributed to the ion exchange process, in which Ni(II) ions replace Na ions at the resin's active sites. This exchange alters the local chemical environment, weakening the vibrational modes that contribute to the Raman signal. Additionally, as Ni(II) ions form a layer on the resin surface, they can interfere with Raman scattering, further reducing the overall

signal intensity. Changes in chemical bonding between Ni(II) and functional groups on the resin, such as the iminodiacetic groups in Lewatit® MonoPlus TP 207, may modify the electron density distribution, further contributing to the observed decrease in peak intensity (Figure 5a).

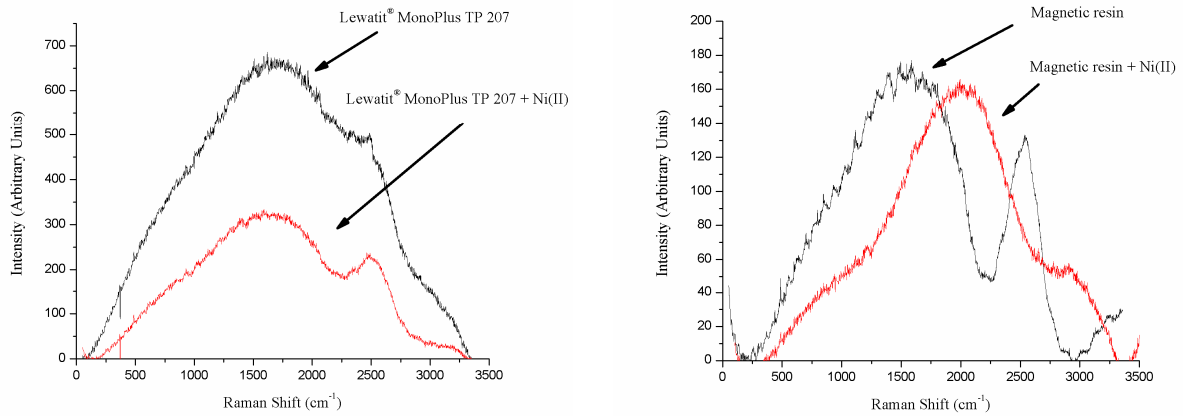


(**a**) (**b**)

**Figure 5.** Raman spectra of (**a**) the chelating ion exchange resin Lewatit® MonoPlus TP 207 before and after the sorption of Ni(II); (**b**) the magnetic resin before and after the sorption of Ni(II).

When comparing the spectra of the magnetic resin before and after Ni(II) adsorption, a slight shift toward higher wavenumbers suggests that Ni(II) adsorption alters bond lengths within the resin, likely due to the formation of coordination complexes between the ions and the functional groups. The presence of magnetite nanoparticles may also affect the local magnetic and electronic environment, leading to changes in the vibrational characteristics of the resin, as reflected in the peak shifts (Figure 5b). Although the highly amorphous nature of the resin tends to obscure sharp peaks, the observed spectral shifts and decreased intensity provide strong evidence of successful Ni(II) sorption, indicating significant interactions between the ions and the resin matrix.

The values for low-frequency mass susceptibilities, presented in Table 3, may be slightly overestimated due to the non-uniform packing of the samples in the measurement boxes. This issue, combined with the significant amount of air trapped within the samples, likely led to an underestimation of the density values ($\rho$), which, in turn, affected the accuracy of the mass susceptibility values. Despite these limitations, the results are in agreement with previously reported data in the literature [66,67], providing a reasonable basis for assessing the magnetic properties of the examined samples.

**Table 3.** Results of magnetic susceptibility measurements with the evaluation of density and magnetic properties of samples.

| Sample Description | Mass [g] | ρ = m/V [kg/m$^3$] | k [$10^{-4}$ SI] | $\chi_{lf}$ $\times 10^{-3}$ [m$^3$/kg] | Magnetic Status |
|---|---|---|---|---|---|
| Magnetite | 6.2873 | 982.4 | 9038 | 0.9200 | Ferromagnetic |
| Magnetic resin | 5.4391 | 849.9 | 37 | 0.0044 | Paramagnetic |

From the data in Table 3, it is clear that magnetite exhibits ferromagnetic behavior, as indicated by its high mass susceptibility ($\chi$lf = 0.9200 $\times$ $10^{-3}$ m$^3$/kg) and a volume susceptibility ($k$) value of 9038 $\times$ $10^{-4}$ SI. In contrast, the magnetic resin samples exhibit much lower mass susceptibilities, with $\chi$lf values of 0.0044 $\times$ $10^{-3}$ m$^3$/kg. These lower susceptibilities, along with the low $k$ values, suggest that the resins are paramagnetic.

It is also worth noting that the magnetic properties of the magnetic resin were preserved despite the incorporation of magnetite nanoparticles. This observation is consistent with the characterization data, which showed that the surface morphology of the resin remained largely unchanged following the modification process. However, the slight reduction in susceptibility compared to pure magnetite can be attributed to the dilution effect caused by the resin matrix, which limits the concentration of magnetic particles.

### *3.2. Adsorption Performance*

#### 3.2.1. Adsorption Kinetics

To evaluate the optimum contact time for the adsorption of Ni(II) metal ions on Lewatit® MonoPlus TP 207 and magnetic resin, metal ions adsorption capacities were determined as a function of time. The adsorption's time course of Ni(II) metal ions on Lewatit® MonoPlus TP 207 and magnetic resin as $q_t$ vs. t is shown in Figure S1. Both materials experienced efficient Ni(II) adsorption processes, taking 6 h for Lewatit® MonoPlus TP 207 to reach a state of equilibrium (over 94.5% of the overall removal occurred within 170 min, for initial concentration of nickel in solution (1 mg/L)). On the other hand, the adsorption reaction of Ni(II) for magnetic resin was faster than that of commercial resin, taking 3 h to reach a state of equilibrium (Figure 6).

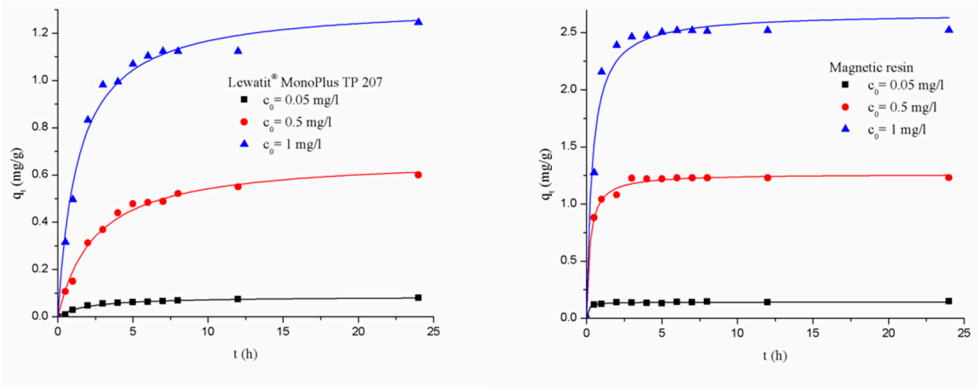


(**a**) (**b**)

**Figure 6.** Adsorption kinetic plots for the removal of Ni(II) using (**a**) Lewatit® MonoPlus TP 207 resin and (**b**) magnetic resin, modeled with a pseudo-second-order kinetic model. The experimental conditions for both plots include a resin dosage of 0.5 mL/L, pH 7 ± 0.2, contact time ranging from 0.5 to 24 h, agitation speed of 120 rpm, and temperature of 298 ± 2 K.

Therefore, during the entire studied time range, the $q_t$ values were: 0.62 mg/g (94.5%), 0.52 mg/g (67.9%) and 1.12 mg/g (77.7%) (Lewatit® MonoPlus TP 207), 0.14 mg/g (89.3%), 1.23 mg/g (98.6%) and 2.5 mg/g (97.9%) (magnetic resin) for the initial nickel concentrations of 0.005; 0.5 and 1 mg/L, respectively. The quantity of adsorbed Ni(II) onto chelating cation-exchangers increases with time. Given how quickly equilibrium was achieved, the emphasis is placed on the modified resin due to the reduction in the time interval during which the adsorption equilibrium is achieved: 3 h. The adsorption capacity of Ni(II) on magnetic resin was higher than Lewatit® MonoPlus TP 207, which was caused by the surface modification (coating) of Lewatit® MonoPlus TP 207 with $Fe_3O_4$ nanoparticles. Some studies have confirmed that in the presence of magnetic particles in various adsorbents, the efficiency of metal adsorption increases [27,68].

The adsorption kinetics were evaluated using pseudo-first-order, pseudo-second-order, and Elovich models to understand the mechanisms governing Ni(II) adsorption on both commercial and magnetic resins (Table S1). The pseudo-first-order model assumes that the rate of occupation of adsorption sites is proportional to the number of unoccupied sites, typically describing physisorption processes. In contrast, the pseudo-second-order model presumes that chemisorption is the rate-limiting step, with the adsorption rate dependent

on the square of the number of unoccupied sites, indicating stronger interactions between the adsorbate and adsorbent. The Elovich model is particularly useful for describing chemisorption on heterogeneous surfaces, often applied when adsorption rates decrease over time, suggesting multilayer adsorption or increasing activation energy as surface saturation occurs [69].

The fitting of experimental data to these kinetic models was carried out, and the results are included in the supplementary table (Figure S2 and Table S2). Based on the correlation coefficients and model fitting, we found that the adsorption of Ni(II) onto both Lewatit® MonoPlus TP 207 and the magnetic resin is best described by the pseudo-second-order model for both resins (Figure 6). This suggests that chemisorption is the dominant mechanism, involving valence forces through the sharing or exchange of electrons between the resin's functional groups and Ni(II) ions. The pseudo-second-order model's strong correlation aligns with chemisorption processes, indicating specific interactions between Ni(II) and the functional groups on the resin surfaces [70]. Furthermore, the values of $k_2$ were 5.9426, 0.6016, 0.5625 (0.05, 0.5, and 1 mg/L) for Lewatit® MonoPlus TP 207 and 66.928, 3.612, 1.011 (0.05, 0.5, and 1 mg/L) for magnetic resin, respectively. The higher $k_2$ values of the magnetic resin indicate a faster adsorption rate and the presence of more active or efficient adsorption sites, facilitating quicker binding of nickel ions. This also suggests stronger interactions between the nickel ions and the magnetic resin, consistent with chemisorption processes, where chemical bonds or electron sharing play a significant role in the adsorption mechanism. Overall, Ni(II) ions can be adsorbed onto the resin through several mechanisms, including surface complication, electrostatic interactions, and ion exchange [71]. These interactions likely contribute to the stronger and more specific binding of Ni(II) on the modified magnetic resin, enhancing its overall adsorption capacity compared to that of the unmodified resin.

### 3.2.2. Adsorption Isotherms

The Langmuir and Freundlich isotherm models were used to evaluate the equilibrium characteristics of Ni(II) adsorption onto iminodiacetate chelating resin and modified magnetic resin at the optimum pH and 25 °C, as depicted in Figure 7. The isotherm parameters are summarized in Table 4. The equations of these models are provided in the Supplementary Materials (Table S1).

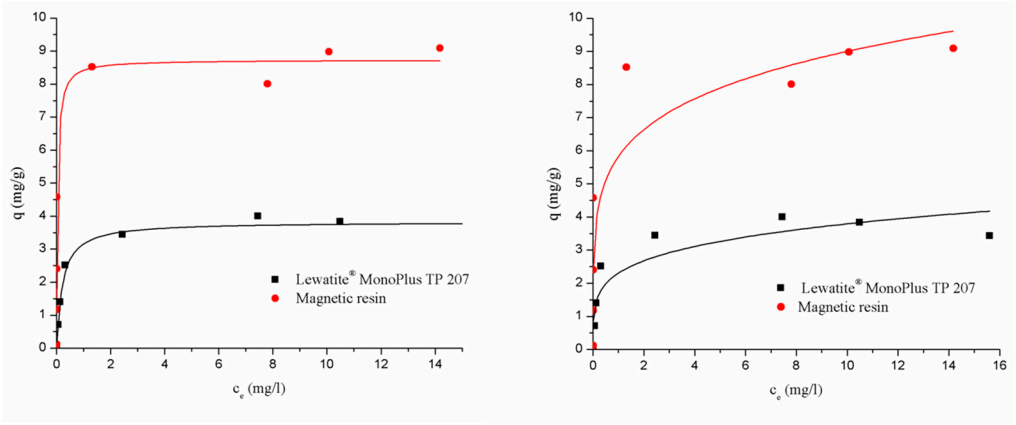


**Figure 7.** Isotherm plots of Ni(II) adsorption on Lewatit® MonoPlus TP 207 and magnetic resin, fitted with the (**a**) Langmuir isotherm model and (**b**) Freundlich isotherm model. The initial concentration of Ni(II) ranged from 0.05 to 20 mg/L, with a resin dosage of 0.5 mL/L. Experiments were conducted at pH 7 ± 0.2, with contact times between 0.5 and 24 h, an agitation speed of 120 rpm, and a temperature of 298 ± 2 K.

**Table 4.** Parameters of Langmuir and Freundlich, isotherms for ion exchange of Ni(II) on the on Lewatit® MonoPlus TP 207 and magnetic resin.

| | Langmuir Isotherm | | | | Freundlich Isotherm | | |
|---|---|---|---|---|---|---|---|
| | $q_{max}$ (mg/g) | $K_L$ (L/mg) | $R^2$ | $R_L$ | n | $K_F$ (mg/g)/(mg/L)$^n$ | $R^2$ |
| Lewatit® MonoPlus TP 207 | 18.13 | 4.74 | 0.9801 | 0.79–0.012 | 0.216 | 2.305 | 0.8059 |
| Magnetic resin | 229.4 | 26.26 | 0.8720 | 0.42–0.002 | 5.825 | 0.188 | 0.7892 |

The Langmuir isotherm model assumes monolayer adsorption on a homogeneous surface, where all binding sites are identical and energetically equivalent. This model implies that once a site is occupied by a molecule, no further adsorption can take place at that site, leading to the formation of a monolayer. The Langmuir model provides an insight into the maximum adsorption capacity and the affinity between the adsorbate and adsorbent. In contrast, the Freundlich isotherm model is empirical and describes adsorption on heterogeneous surfaces, allowing for multilayer adsorption. This model suggests that the adsorption energy decreases logarithmically as the coverage increases, making it suitable for systems with varying adsorption site energies. The Freundlich isotherm model, in contrast, describes adsorption on heterogeneous surfaces, allowing for multilayer adsorption. The model suggests that adsorption sites have varying energies, and stronger binding sites are occupied first, followed by weaker binding sites. The Freundlich constant n provides an indication of adsorption intensity, where n > 1 suggests favorable adsorption. This model is particularly suitable for systems with a heterogeneous surface or where the adsorption heat decreases as coverage increases [72].

Based on the modeling data, the correlation coefficients ($R^2$) reveal that the adsorption process fits the Langmuir model better ($R^2$ = 0.8720–0.9801) compared to the Freundlich model (0.7892–0.8059), especially for the modified magnetic resin. This indicates that adsorption predominantly occurs as a monolayer on a homogeneous surface, which aligns with the uniform distribution of $Fe_3O_4$ on the resin and the properties of the chelating resin.

The magnetic resin demonstrated a significantly higher adsorption capacity ($q_{max}$ = 229.4 mg/g) compared to Lewatit® MonoPlus TP 207 ($q_{max}$ = 18.13 mg/g). This drastic difference highlights the effect of magnetite nanoparticle modification, which greatly enhances the resin's capacity for nickel ion removal. The increased surface area and additional active sites provided by the magnetic particles enhance nickel ion removal. The Langmuir constant ($K_L$), representing the affinity between Ni(II) and the resin, was notably higher for the magnetic resin (26.26 L/mg) compared to Lewatit® MonoPlus TP 207 (4.74 L/mg). This suggests that the magnetic resin has a much stronger interaction with Ni(II) ions, further reinforcing its suitability for heavy metal removal from water.

The separation factor ($R_L$) values, which describe the favorability of the adsorption process, fall between 0 and 1 for both resins, indicating favorable adsorption conditions [73–75]. The $R_L$ values for Lewatit® MonoPlus TP 207 range from 0.79 to 0.012, while for the magnetic resin, they range from 0.42 to 0.002. These values confirm that Ni(II) adsorption is more favorable at lower initial concentrations for both resins, with the magnetic resin showing enhanced performance even at higher concentrations. The initial concentration of Ni(II) in this experiment ranged from 0.05 to 20 mg/L, allowing us to evaluate the adsorption behavior of both resins across a broad range of concentrations, from low to high.

### *3.3. Proposed Mechanism of Ni(II) Removal by Commercial Resin and Magnetic Resin*

Chelating resins, such as Lewatit® MonoPlus TP 207, are ion-exchange resins with iminodiacetic functional groups that selectively form complexes with metal ions through chelation. The iminodiacetate group, consisting of two carboxyl groups and one nitrogen atom, enables Ni(II) removal via ion exchange and chelation. Additionally, the nitrogen atom functions as a Lewis base, enabling the formation of a ligand bond with the metal

cation (which acts as a Lewis acid). Initially, Ni(II) forms weak ionic pairs with the carboxylate groups, which then transition into stronger complexes as water molecules are displaced. This is supported by changes in the FTIR spectrum (Figure 4a), particularly the reduction in peak intensity at 3440 $cm^{-1}$, indicating active involvement of the iminodiacetate groups in Ni(II) binding through coordination or chelation. The EDS analysis further supports this as it reveals changes in elemental composition after Ni(II) sorption (Figure 2c), confirming that ion exchange is a significant contributor to the adsorption mechanism. Overall, the combined evidence from FTIR and EDS suggests that Ni(II) removal by Lewatit® MonoPlus TP 207 is primarily driven by chelation through iminodiacetate groups and is facilitated by ion-exchange interactions (Figure 8a).

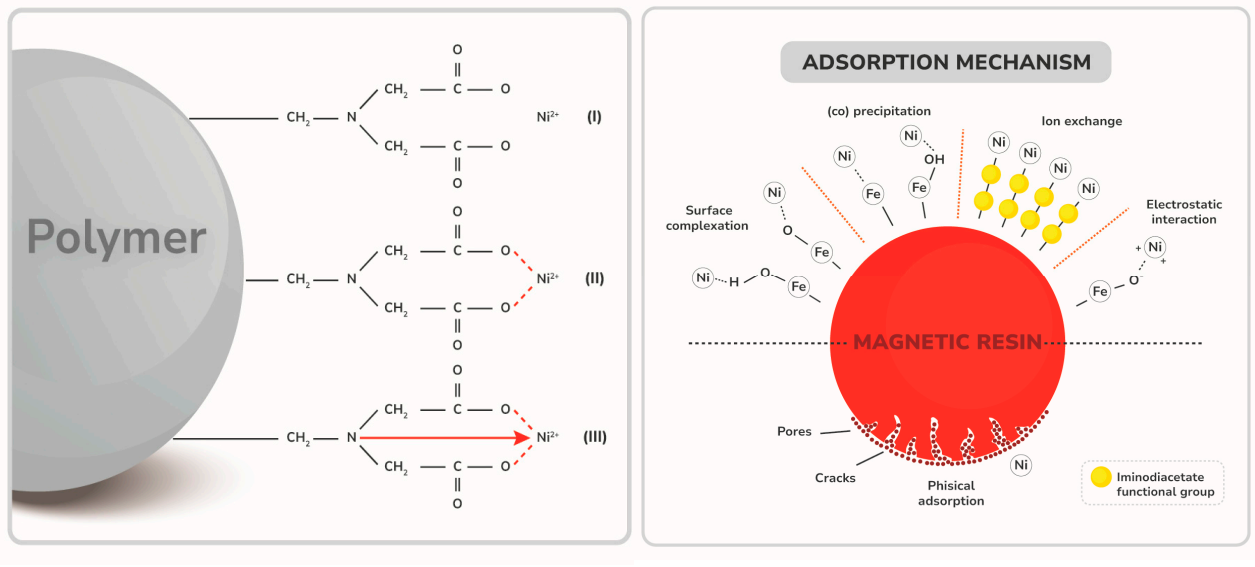


(**a**) (**b**)

**Figure 8.** Proposed mechanism of nickel removal using (**a**) Lewatit® MonoPlus TP 207 resin and (**b**) magnetic resin.

The sorption mechanism of Ni(II) by the newly synthesized magnetic resin involves a combination of the chelating properties of the iminodiacetate groups in Lewatit® MonoPlus TP 207 and interactions facilitated by the embedded $Fe_3O_4$ nanoparticles (Figure 8b). In addition to the traditional ion exchange and chelation processes observed in the commercial resin, the magnetic resin benefits from mechanisms such as surface complexation, coprecipitation, and electrostatic interactions [76]. As shown in Section 3.2.2, the $Fe_3O_4$ nanoparticles significantly enhance the resin's capacity to remove Ni(II) ions by providing additional sorption sites through three key interactions:

(a) Surface Complexation: This process includes both specific and non-specific sorption. Specific adsorption results in the formation of inner-sphere complexes, where Ni(II) ions bond directly to the magnetite surface via ligand exchange, leading to strong binding with the Fe-OH groups. Non-specific adsorption, on the other hand, forms outer-sphere complexes, where Ni(II) ions are indirectly bound to the resin surface through water molecules. These interactions, while weaker than inner-sphere complexes, still contribute significantly to the overall sorption capacity.

The FTIR spectrum reveals changes after Ni(II) sorption, confirming these interactions. A strong peak at 520 $cm^{-1}$ (Fe-O stretching vibrations) indicates the active role of magnetite in Ni(II) adsorption, while increased intensities at 3440 $cm^{-1}$, 1626 $cm^{-1}$, and 1400 $cm^{-1}$ suggest that both the iminodiacetate functional groups and $Fe_3O_4$ nanoparticles enhance the sorption capacity. Additionally, a band at 709 $cm^{-1}$ suggests metal–oxygen coordination and further interactions facilitated by the modified resin surface (Figure 4b). EDS analysis supports this mechanism, showing no significant decrease in iron or sodium content after

Ni(II) adsorption, which implies the existence of a combined mechanism of ion exchange and surface complexation (Figure 2d).

(b) (Co)Precipitation: At higher pH levels, coprecipitation occurs, where Ni(II) ions form hydroxide precipitates with $Fe_3O_4$, enhancing the sorption process. This coprecipitation mechanism significantly aids in Ni(II) removal, particularly in conditions favoring the formation of Ni(II) hydroxides.

(c) Electrostatic interactions: In aqueous solutions, Ni(II) ions interact with oxygen atoms in the magnetite phase. During adsorption, $H^+$ ions are displaced from the adsorbent functional groups, allowing Ni(II) to bind to the surface through electrostatic attraction.

(d) Electrostatic interactions are particularly effective when the surface of the adsorbent is negatively charged at the operating pH, promoting the attraction of the positively charged Ni(II) ions to the surface.

The combination of ion exchange, chelation, and the incorporation of magnetite nanoparticles significantly enhances the sorption efficiency for Ni(II) removal. The magnetite phase introduces additional binding sites, which contribute to both ion exchange and surface adsorption processes. This synergy between the magnetite and resin phases optimizes the adsorption capacity, resulting in a highly efficient and effective magnetic resin for Ni(II) removal.

### *3.4. DSD Model Evaluation and Process Optimization*

In order to examine the influence of various process parameters, including pH, contact time, resin dosage, nickel, calcium and magnesium concentration on nickel removal efficiency, DSD statistical analysis was applied. Since the number of experiments N for DSD is 2k + 1, a total number of experimental runs was 28, including 13 experiments performed in replication with two additional central points [56]. The six-variable DSD matrix and nickel removal efficiency (%) values obtained in the experiment with Lewatit® MonoPlus TP 207 and magnetic resin are presented in Table S3. The higher range of nickel removal efficiency was established using Lewatit® MonoPlus TP 207 (33.0–99.8%). The maximum nickel removal efficiency was found to be 99.8% and 99.42% with Lewatit® MonoPlus TP 207 and magnetic resin, respectively.

DSD analysis was performed by JMP's stepwise regression control tool, resulting in a large number of regression models. A few candidate models were selected, but the most efficient regression model, which would provide the best fit for the experimental data, was selected based on the standard descriptive factors (coefficient of determination, adjusted coefficient of determination), as well as by calculation of corrected Akaike Information Criterion (AIC), Bayesian Information Criterion (BIC) and Root Means Square Error (RMSE). Based on the summary of fit (Table S4), the adopted regression models explain 87–95% of variance in the observed nickel removal values for all investigated resins, implying a good approximation of the experimental data with the selected models, while the rest of 5–13% of the total variance is not covered by the model. The percentage of fluctuation in the response is reflected through the R-square values, while a small RMSE value in comparison to the mean of response indicates a good fit and accuracy of model prediction [77,78]. The quality of an individual model, relying on good approximation and simplicity, is evaluated by the AIC parameter. Inadequate data fitting has been avoided by observing BIC values parameter. The best ability to predict the regression model is achieved based on the selection of lower AIC and BIC values, respecting the simplicity of the model as an additional criterion [78].

Furthermore, the significance and the validity of the regression model was confirmed based on the ANOVA test result (Table S5), as shown in the rightmost column (F ratio). The demonstrated model F-ratios of 10.15 and 23.04 for Lewatit® MonoPlus TP 207 and magnetic resin, respectively, and the low $p$-value (<0.0001) indicate that the model is highly significant for the nickel removal efficiency, at a 95% of confidence level.

Estimated regression coefficients sorted by ascending order of $p$-values are presented in Table S6. For nickel removal efficiency, contact time exhibits statistical significance within

the usage of both resins, which reflects in the magnitude of its estimate. The pronounced influence of contact time is also shown in the optimization diagram presented in the following text. Furthermore, in the experiment with Lewatit® MonoPlus TP 207, nickel concentration is shown to be one of the main significant parameters. This is corroborated by the optimization plot, which reveals that optimum nickel removal efficiency is obtained when nickel concentration lies between the center and high level, i.e., 110–120 µg/L. The sign before the linear term of nickel concentration is positive, which suggests that the increase in nickel concentration contributes to its removal efficiency up to a certain point, after which further increase has an adverse effect on the removal process. Moving in both directions away from this optimal point has a pronounced effect on process efficiency, causing its reduction.

Although not statistically significant as main parameter within the Lewatit® MonoPlus TP 207 experiment, pH is involved in two significant interactions: with nickel concentration (Figure 9a) and magnesium concentration (Figure 9b).

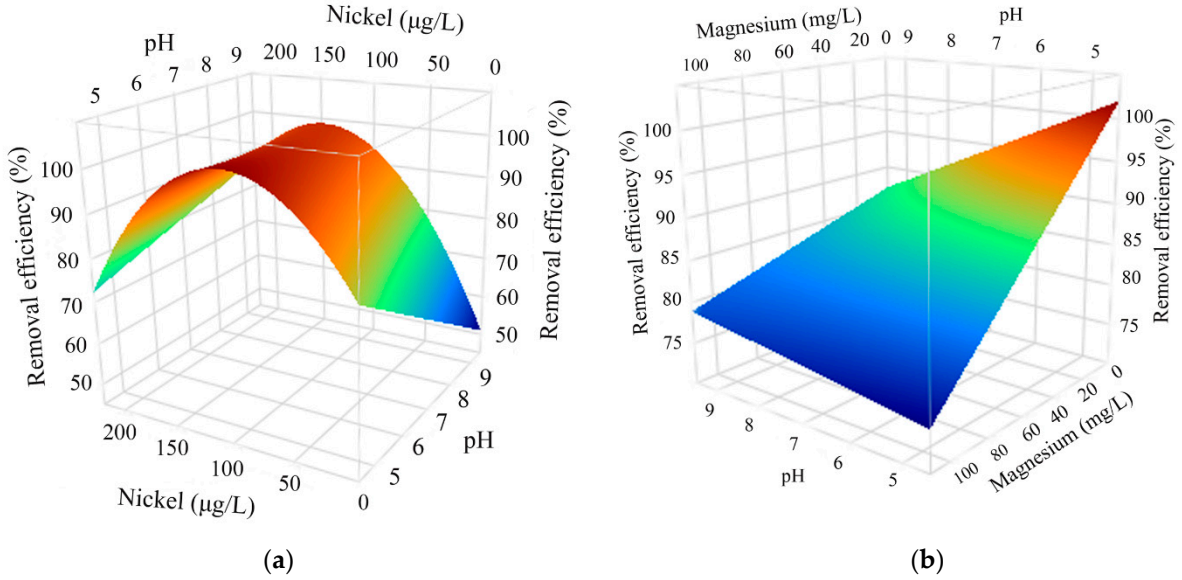


**Figure 9.** Surface response plots illustrating two significant interactions in the regression model: (**a**) pH × nickel concentration; (**b**) pH × magnesium concentration.

The surface response plot implies that at both low and high pH values, the nickel removal efficiency by ion exchange increases with the increase in its initial concentration, up to a certain upper limit of 110 µg/L, which is also established in the optimization diagram (Figure 10a). A further increase in the initial nickel concentration led to a decrease in terms of its removal. In addition, it was observed that at lower pH values, due to the significant two-way interaction, a higher nickel removal degree by ion exchange is achieved. This can be explained by the fact that at pH values lower than 7.41, nickel predominantly appears in the form of $Ni^{2+}$, favoring the ion exchange of $H^+$ and $Ni^+$. In contrast, at higher pH values (above pH = 8) nickel is predominantly present in the form of hydrated ions $Ni(OH)^{+1}$ and $Ni(OH)_2{}^0$, implying that the ion exchange process itself is unfavorable [59].

Both pH and magnesium concentration are statistically significant main parameters for the nickel removal process with magnetic resin, which, at the same time, achieve a significant two-way interaction. pH maintained at a low level has the most pronounced effect on the influence of magnesium concentration on nickel removal. The surface response plot (Figure 10b) indicates that maximum nickel removal efficiency is achieved when the magnesium concentration is reduced from 100 to 20 mg/L, while the pH is kept at low level.

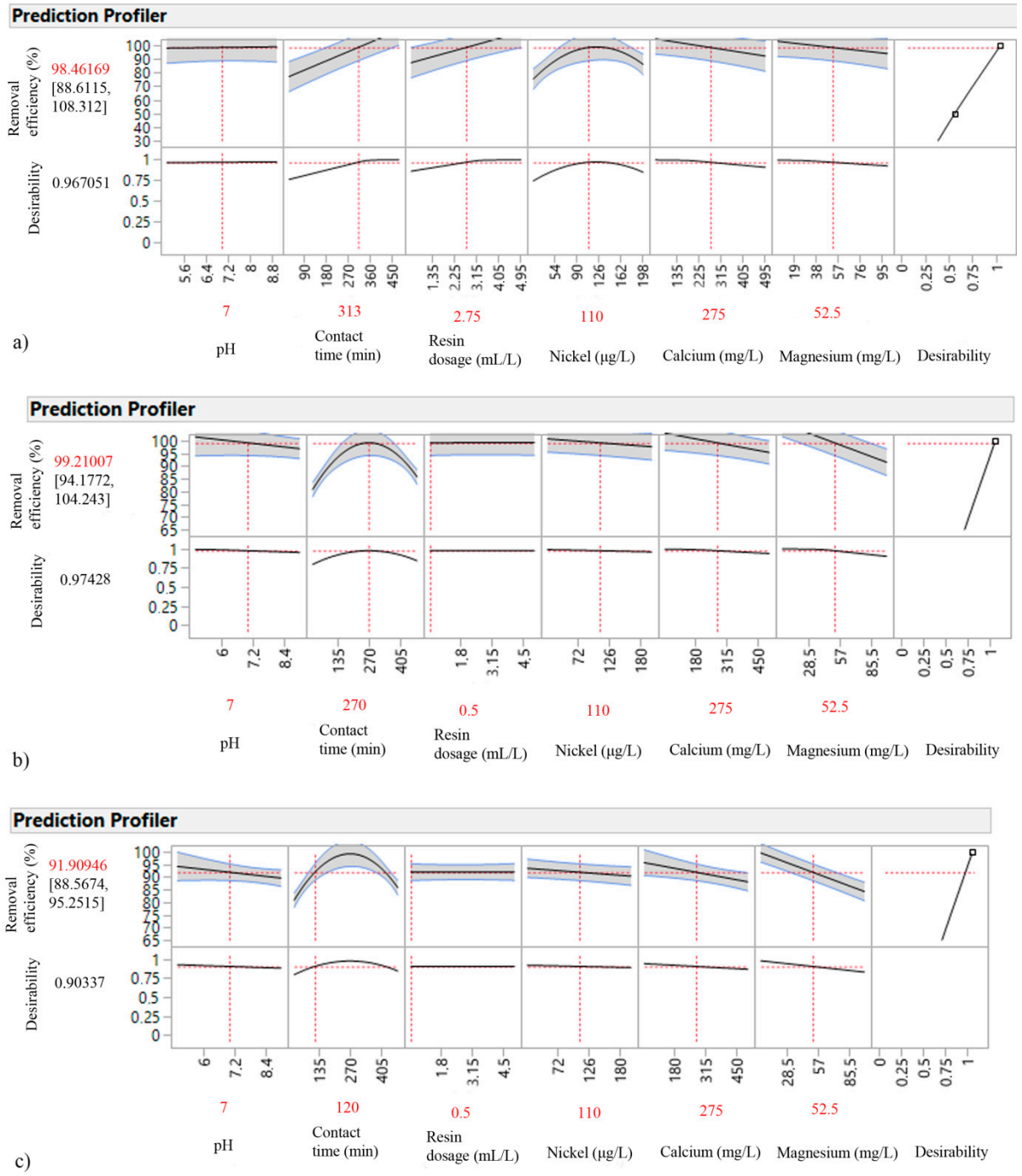


**Figure 10.** Optimization diagrams for nickel removal with: (**a**) Lewatit® MonoPlus TP 207; (**b**) magnetic resin at 270 min; (**c**) magnetic resin at 120 min.

For instance, $Ni^{2+}$ and $Mg^{2+}$ both have positive charges but differ in size and charge density. Nickel ions generally have a higher charge density compared to magnesium ions. This means that $Ni^{2+}$ might have a stronger affinity for the ion exchange sites on the resin. But in acidic conditions, the concentration of hydroxide ions ($OH^-$) decreases, and magnesium remains in its ionic form as $Mg^{2+}$ because there are not enough $OH^-$ ions to precipitate it as magnesium hydroxide. Therefore, at low pH, magnesium is typically found as $Mg^{2+}$ ions in solution, and competition between nickel and magnesium ions can lead to decreased efficiency in removing $Ni^{2+}$ [77–79]. In summary, this means that both pH and magnesium concentration are important for optimizing nickel removal, and

their combined effect must be considered. The interaction between these parameters can significantly alter the process's efficiency, with pH playing a key role in how magnesium concentration impacts nickel removal.

Since the capability and adaptability of JMP 13 software provide significant advances in process optimization, the main goal of this study's experimental design is based on maximizing the efficiency of nickel removal process in relation to process conditions, detailed in Table S3. The optimization diagrams for ion exchange process are shown in Figure 10, where the effect of main factors, marked by a vertical red dashed line, can be most easily observed. The six cells on the graph illustrate how the nickel removal efficiency changes as a function of one variable, while all other variables remain constant.

The highest efficiency within Lewatit® MonoPlus TP 207 of 98.46% was proposed under the following optimal conditions: pH of 7, contact time of 313 min, resin dosage of 2.75 mL/L, nickel concentration of 110 μg/L, calcium concentration of 275 mg/L and magnesium concentration of 52.5 mg/L (Figure 10a). Furthermore, 99.21% of nickel removal efficiency (Figure 10b) was obtained by application of magnetic resin under the same process conditions, with a significant difference in reduced contact time (270 min) and resin dosage (0.5 mL/L). A look at the optimization profiles reveals that the obtained results are correlated with established main parameters and two-way interactions, implying that contact time contributes the most to the removal efficiency process. Since longer contact time (270–313 min) is unfavorable from the technoeconomic aspect, the suitability of JMP 13 software enables the variation in optimal values, giving an insight into the change in process efficiency in order to improve the operational conditions of the process itself. Therefore, by reducing the contact time from 270 to 120 min (Figure 10c), the efficiency of the process might be slightly reduced (up to 7%), but from the aspect of real application, the results are certainly promising. The results obtained indicate that the usage of magnetic resin within the lowest dosage (0.5 mL/L) could provide a cost-effective and highly efficient process with a nickel removal efficiency of 92%.

Furthermore, experimental verification of the predicted optimal response was performed in order to verify the nickel removal efficiency optimized by the adopted regression model. For that purpose, eight additional experiments at the theoretical point of optimum were conducted. Based on the results obtained (Table S7), a 95% confidence interval was calculated (Figure S3). The nickel removal efficiency values of 98% and 92%, optimized by the adopted regression model (Figure 10a,c), obviously fit the confirmatory run confidence interval, meaning that that the regression model adopted describes well the nickel removal process with cation exchange resin, and that the model was successful.

## 4. Conclusions

We developed a magnetic resin by coating Lewatit® MonoPlus TP 207 ion-exchange resin beads with hexagonal magnetite crystals, confirmed by XRD, FTIR, and magnetic susceptibility measurements. The magnetic resin demonstrated high adsorption capacity for nickel ions, with easy separation using a magnetic field, outperforming other magnetic adsorbents reported in the literature. The use of DSD statistical analysis revealed optimal conditions for nickel removal, achieving a 99.21% efficiency with the magnetic resin at a lower dosage (0.5 mL/L) and reduced contact time (270 min) compared to the unmodified resin. Although reducing the contact time to 120 min slightly decreased efficiency (~7%), the results remain promising for practical applications, offering an efficient and cost-effective solution for nickel removal.

Future work should focus on optimizing the process for large-scale applications, specifically by reducing contact times while maintaining high efficiency. Additionally, assessing the selectivity of the magnetic resin for Ni(II) ions in the presence of other metal ions is crucial for practical water treatment scenarios, as it will provide an insight into its performance in complex water matrices. To bridge the gap between laboratory-scale findings and real-world applications, performance tests under continuous-flow conditions are necessary to better reflect industrial settings. Furthermore, testing the resin with

real water samples containing natural metal concentrations will provide a more accurate assessment of its performance in diverse scenarios.

For sustainable and practical implementation, evaluating the recyclability and long-term stability of the magnetic resin is essential, along with scaling up synthesis. Moreover, designing and constructing effective magnetic separation systems will be critical for efficient deployment in large-scale operations. The development of pilot and full-scale magnetic separation systems is necessary to demonstrate the feasibility of magnetic resins in industrial water treatment.

**Supplementary Materials:** The following supporting information can be downloaded at: https://www.mdpi.com/article/10.3390/pr12102287/s1, Figure S1: Adsorption of Ni(II) onto Lewatit® MonoPlus TP 207 and magnetic resin as a function of contact time under varying initial concentrations: (a) 0.05 mg/L, (b) 0.5 mg/L, and (c) 1 mg/L. Experimental conditions: resin dosage = 0.5 mL/L, solution volume = 500 mL (synthetic water matrix containing Ni(II)), pH = 7.0 ± 0.2, contact time = 30 min to 24 h, agitation speed = 120 rpm, temperature = 298 ± 2 K; Figure S2: Kinetic plots for Ni(II) adsorption onto Lewatit® MonoPlus TP 207 and magnetic resins under various kinetic models. (a) Pseudo-first-order model for Lewatit® MonoPlus TP 207 resin; (b) Elovich model for Lewatit® MonoPlus TP 207 resin; (c) pseudo-first-order model for magnetic resin; (d) Elovich model for magnetic resin. Experimental conditions: resin dosage = 0.5 ml/l mg, solution volume = 500 mL (synthetic water matrix containing Ni(II)), pH = 7.0 ± 0.2, contact time = 30 min to 24 h, agitation speed = 120 rpm, temperature = 298 ± 2 K); Figure S3: Verification diagram for: (a) Lewatit® MonoPlus TP 207; (b) magnetic resin. Table S1: Mathematical models used for modelling data obtained in kinetic and isotherm adsorption experiments; Table S2: Kinetic parameters for the sorption of Ni(II) onto Lewatit® MonoPlus TP 207 and magnetic resin; Table S3: DSD experimental design layout and nickel removal efficiency; Table S4: Summary of fit; Table S5: Analysis of variance and "lack of fit" test; Table S6: Estimated regression coefficients of the significant main and interaction effects; Table S7: Experimental verification of optimized ion exchange processes.

**Author Contributions:** M.M.: Conceptualization, investigation, writing—original draft preparation; J.N.: investigation, formal analysis, writing—review and editing; V.G.: formal analysis, writing—original draft preparation; J.P.: investigation, formal analysis, visualization; Ž.C.: formal analysis, visualization; A.T.: formal analysis, visualization; J.A.: conceptualization, investigation, writing—review and editing funding acquisition. All authors have read and agreed to the published version of the manuscript.

**Funding:** The authors gratefully acknowledge the financial support of the Ministry of Science, Technological Development and Innovation of the Republic of Serbia (Grants No. 451-03-66/2024-03/200125 and 451-03-65/2024-03/200125).

**Data Availability Statement:** The raw data supporting the conclusions of this article will be made available by the authors on request.

**Conflicts of Interest:** The authors have no relevant financial or non-financial interests to disclose.

## References

1. Basheer, A.A. New generation nano-adsorbents for the removal of emerging contaminants in water. *J. Mol. Liq.* **2018**, *261*, 583–593. [CrossRef]
2. Vakili, M.; Rafatullah, M.; Yuan, J.; Zwain, H.M.; Mojiri, A.; Gholami, Z.; Gholami, F.; Wang, W.; Giwa, A.S.; Yu, Y.; et al. Nickel ion removal from aqueous solutions through the adsorption process: A review. *Rev. Chem. Eng.* **2020**, *37*, 755–778. [CrossRef]
3. Hussain, C.M.; Keçili, R. Environmental pollution and environmental analysis. In *Modern Environmental Analysis Techniques for Pollutants*; Hussain, C.M., Keçili, R., Eds.; Elsevier: Amsterdam, The Netherlands, 2020; pp. 1–36.
4. Deng, Y.; Shi, H.; Yu, X.; Penghui, S.; Liming, Y.; Yu, K.; Keke, H.; Xubiao, L. Simultaneous Heavy Metals Removal via in Situ Construction of Multivariate Metal-Organic Gels in Actual Wastewater and the Reutilization for Sb(V) Capture. *Chem. Eng. J.* **2020**, *400*, 125359. [CrossRef]
5. Schaumlöfel, D. Nickel species: Analysis and toxic effects. *J. Trace Elem. Med. Biol.* **2012**, *26*, 1–6. [CrossRef] [PubMed]
6. Zambelli, B.; Uversky, V.N.; Ciurli, S. Nickel impact on human health: An intrinsic disorder perspective. *Biochim. Biophys. Acta Proteins Proteom.* **2016**, *1864*, 1714–1731. [CrossRef]
7. Rinklebe, J.; Antoniadis, V.; Shaheen, S.M.; Rosche, O.; Altermann, M. Health risk assessment of potentially toxic elements in soils along the Central Elbe River, Germany. *Environ. Int.* **2019**, *126*, 76–88. [CrossRef]

8. Shaheen, S.M.; El-Naggar, A.; Antoniadis, V.; Moghanm, F.S.; Zhang, Z.; Tsang, D.C.W.; Ok, Y.S.; Rinklebe, J. Release of toxic elements in fishpond sediments under dynamic redox conditions: Assessing the potential environmental risk for a safe management of fisheries systems and degraded waterlogged sediments. *J. Environ. Manag.* **2020**, *255*, 109778. [CrossRef] [PubMed]
9. International Agency for Research on Cancer IARC. *Monographs on the Identification of Carcinogenic Hazards to Human*; International Agency for Research on Cancer IARC: Lyon, France, 2020.
10. Directive (EU) 2020/2184 of the European Parliament and of the Council of 16 December 2020 on the Quality of Water Intended for Human Consumption. Available online: https://eur-lex.europa.eu/eli/dir/2020/2184/oj (accessed on 5 September 2024).
11. Schrenk, D.; Bignami, M.; Bodin, L.; Chipman, J.K.; del Mazo, J.; Grasl-Kraupp, B.; Hogstrand, C.; Hoogenboom, L.; Leblanc, J.; Nebbia, C.S.; et al. Update of the risk assessment of nickel in food and drinking water. *EFSA J.* **2020**, *18*, 6268. [CrossRef]
12. World Health Organization (WHO). *Guidelines for Drinking-Water Quality: Fourth Edition Incorporating the First Addendum*; WHO: Geneva, Switzerland, 2018.
13. Kumar, R.; Rauwel, P.; Rauwel, E. Nanoadsorbants for the Removal of Heavy Metals from Contaminated Water: Current Scenario and Future Directions. *Processes* **2021**, *9*, 1379. [CrossRef]
14. Tahoon, M.A.; Siddeeg, S.M.; Salem Alsaiari, N.; Mnif, W.; Ben Rebah, F. Effective Heavy Metals Removal from Water Using Nanomaterials: A Review. *Processes* **2020**, *8*, 645. [CrossRef]
15. Dhanda, N.; Kumar, S. Smart and Innovative Nanotechnology Applications for Water Purification. *Hybrid Adv.* **2023**, *3*, 100044. [CrossRef]
16. Ali, Q.; Ahmed Zia, M.; Kamran, M.; Shabaan, M.; Zulfiqar, U.; Ahmad, M.; Iqbal, R.; Maqsood, M.F. Nanoremediation for heavy metal contamination: A review. *Hybrid Adv.* **2023**, *4*, 100091. [CrossRef]
17. Ethaib, S.; Al-Qutaifia, S.; Al-Ansari, N.; Zubaidi, S.L. Function of Nanomaterials in Removing Heavy Metals for Water and Wastewater Remediation: A Review. *Environments* **2022**, *9*, 123. [CrossRef]
18. Baby, R.; Hussein, M.Z.; Abdullah, A.H.; Zainal, Z. Nanomaterials for the Treatment of Heavy Metal Contaminated Water. *Polymers* **2022**, *14*, 583. [CrossRef]
19. Castelo-Grande, T.; Augusto, P.A.; Rico, J.; Marcos, J.; Iglesias, R.; Hernández, L.; Barbosa, D. Magnetic Water Treatment in a Wastewater Treatment Plant: Part I—Magnetic Water Treatment in a Wastewater Treatment Plant: Part I—Sorption and Magnetic Particles. *J. Environ. Manag.* **2021**, *281*, 111872. [CrossRef]
20. Castelo-Grande, T.; Augusto, P.A.; Rico, J.; Marcos, J.; Iglesias, R.; Hernández, L.; Barbosa, D. Magnetic Water Treatment in a Wastewater Treatment Plant: Part II—Processing Waters and Kinetic Study. *J. Environ. Manag.* **2021**, *285*, 112177. [CrossRef]
21. Liosis, C.; Papadopoulou, A.; Karvelas, E.; Karakasidis, T.E.; Sarris, I.E. Heavy Metal Adsorption Using Magnetic Nanoparticles for Water Purification: A Critical Review. *Materials* **2021**, *14*, 7500. [CrossRef]
22. Shukla, S.; Khan, R.; Daverey, A. Synthesis and Characterization of Magnetic Nanoparticles, and Their Applications in Wastewater Treatment: A Review. *Environmetal. Technol. Innov.* **2021**, *24*, 101924. [CrossRef]
23. Ali, I.; Peng, C.; Naz, I.; Amjed, M.A. Water Purification Using Magnetic Nanomaterials: An Overview. In *Magnetic Nanostructures. Nanotechnology in the Life Sciences*; Abd-Elsalam, K., Mohamed, M., Prasad, R., Eds.; Springer: Cham, Switzerland, 2019. [CrossRef]
24. Khan, F.S.A.; Mubarak, N.M.; Tan, Y.H.; Karri, R.R.; Khalid, M.; Walvekar, R.; Abdullah, E.C.; Mazari, A.; Nizamuddin, S. Magnetic Nanoparticles Incorporation into Different Substrates for Dyes and Heavy Metals Removal—A Review. *Environ. Sci. Pollut. Res. Int.* **2020**, *27*, 43526–43541. [CrossRef] [PubMed]
25. Goswami, M.K.; Srivastava, A.; Dohare, R.K.; Tiwari, A.K.; Srivastav, A. Recent advances in conducting polymer-based magnetic nanosorbents for dyes and heavy metal removal: Fabrication, applications, and perspective. *Environ. Sci. Pollut. Res. Int.* **2023**, *30*, 73031–73060. [CrossRef]
26. Nikić, J.; Watson, M.; Tubić, A.; Šolić, M.; Agbaba, J. Recent trends in the application of magnetic nanocomposites for heavy metals removal from water: A review. *Sep. Sci. Technol.* **2024**, *59*, 293–331. [CrossRef]
27. Sikora, E.; Hajdu, V.; Muránszky, G.; Katona, K.K.; Kocserha, I.; Kanazawa, T.; Fiser, B.; Viskolcz, B.; Vanyorek, L. Application of ion-exchange resin beads to produce magnetic adsorbents. *Chem. Pap.* **2020**, *75*, 1187–1195. [CrossRef]
28. Liu, B.; Liu, Z.; Wu, H.; Pan, S.; Cheng, X.; Sun, Y.; Xu, Y. Effective and simultaneous removal of organic/inorganic arsenic using polymer-based hydrated iron oxide adsorbent: Capacity evaluation and mechanism. *Sci. Total Environ.* **2020**, *742*, 140508. [CrossRef]
29. Perlova, O.; Dzyazko, Y.; Halutska, I.; Perlova, N.; Palchik, A. Anion exchange resin modified with nanoparticles of hydrated zirconium dioxide for sorption of soluble U(VI) compounds. In *Nanooptics, Nanophotonics, Nanostructures, and Their Applications*; Springer International Publishing: New York, NY, USA, 2018; pp. 3–15. [CrossRef]
30. Manjare, S.B.; Chaudhari, R.A.; Thopate, S.R.; Risbud, K.P.; Badade, S.M. Resin loaded palladium nanoparticle catalyst, characterization and application in –C–C– coupling reaction. *SN Appl. Sci.* **2020**, *2*, 988. [CrossRef]
31. Sodzidzi, Z.; Phiri, Z.; Nure, J.F.; Msagati, T.A.M.; de Kock, L.-A. Adsorption of Toxic Metals Using Hydrous Ferric Oxide Nanoparticles Embedded in Hybrid Ion-Exchange Resins. *Materials* **2024**, *17*, 1168. [CrossRef]
32. Dizge, N.; Keskinler, B.; Barlas, H. Sorption of Ni(II) ions from aqueous solution by Lewatit cation-exchange resin. *J. Hazard. Mater.* **2009**, *167*, 915–926. [CrossRef]
33. Tan, J.; Huang, Y.; Wu, Z.; Chen, X. Ion Exchange Resin on Treatment of Copper and Nickel Wastewater. *IOP Conf. Ser. Earth Environ. Sci.* **2017**, *94*, 012122. [CrossRef]

34. Božecka, A.M.; and Rydlewska, S.S. The use of ion exchangers for removing cobalt and nickel ions from water solutions. *Arch. Min. Sci.* **2018**, *63*, 633–646. [CrossRef] [PubMed]
35. Wołowicz, A.; and Wawrzkiewicz, M. Screening of Ion Exchange Resins for Hazardous Ni(II) Removal from Aqueous Solutions: Kinetic and Equilibrium Batch Adsorption Method. *Processes* **2021**, *9*, 285. [CrossRef]
36. Lebron, Y.A.R.; Moreira, V.R.; Amaral, M.C.S. Metallic ions recovery from membrane separation processes concentrate: A special look onto ion exchange resins. *Chem. Eng. J.* **2021**, *425*, 131812. [CrossRef]
37. Wołowicz, A.; Hubicki, Z. The use of the chelating resin of a new generation Lewatit MonoPlus TP-220 with the bis-picolylamine functional groups in the removal of selected metal ions from acidic solutions. *Chem. Eng. J.* **2012**, *197*, 493–508. [CrossRef]
38. Abbasi, P.; McKevitt, P.; Dreisinger, D.B. The kinetics of nickel recovery from ferrous containing solutions using an Iminodiacetic acid ion exchange resin. *Hydrometallurgy* **2018**, *175*, 333–339. [CrossRef]
39. Ahamad, T.; Naushad, M.; Alshehri, S.M. Fabrication of magnetic polymeric resin for the removal of toxic metals from aqueous medium: Kinetics and adsorption mechanisms. *J. Water Process Eng.* **2020**, *36*, 101284. [CrossRef]
40. Atia, A.A.; Donia, A.M.; Yousif, A.M. Removal of some hazardous heavy metals from aqueous solution using magnetic chelating resin with iminodiacetate functionality. *Sep. Purif. Technol.* **2008**, *61*, 348–357. [CrossRef]
41. Aranda-García, E.; Chávez-Camarillo, G.M.; Cristiani-Urbina, E. Effect of Ionic Strength and Coexisting Ions on the Biosorption of Divalent Nickel by the Acorn Shell of the Oak *Quercus crassipes* Humb. & Bonpl. *Processes* **2020**, *8*, 1229. [CrossRef]
42. Charazińska, S.; Burszta-Adamiak, E.; Lochyński, P. Recent trends in Ni(II) sorption from aqueous solutions using natural materials. *Rev. Environ. Sci. Bio/Technol.* **2022**, *21*, 105–138. [CrossRef]
43. Badawi, A.H.M.; Elkodous, A.; Ali, G.A.M. Recent advances in dye and metal ion removal using efficient adsorbents and novel nano-based materials: An overview. *RSC Adv.* **2021**, *11*, 36528–36553. [CrossRef]
44. Lamidi, S.; Olaleye, N.; Bankole, Y.; Obalola, A.; Aribike, E.; Adigun, I. *Applications of Response Surface Methodology (RSM) in Product Design, Development, and Process Optimization*; IntechOpen: Rijeka, Croatia, 2023. [CrossRef]
45. Reji, M.; Kumar, R. Response surface methodology (RSM): An overview to analyze multivariate data. *Indian J. Microbiol. Res.* **2022**, *9*, 241–248. [CrossRef]
46. Shamkhi, H.A.; Abdulhasan, M.J.; Raheem, S.A.; Al-Zubaidi, H.A.M.; Janabi, A.S.K. Optimization of heavy metals removal from wastewater by magnetic nano-zeolite using response surface methodology. *Desalination Water Treat.* **2023**, *306*, 63–74. [CrossRef]
47. Fertu, D.I.; Bulgariu, L.; Gavrilescu, M. Modeling and Optimization of Heavy Metals Biosorption by Low-Cost Sorbents Using Response Surface Methodology. *Processes* **2022**, *10*, 523. [CrossRef]
48. Sasidharan, R.; Kumar, A. Response surface methodology for optimization of heavy metal removal by magnetic biosorbent made from anaerobic sludge. *J. Indian Chem. Soc.* **2022**, *99*, 9100638. [CrossRef]
49. Khoshraftar, Z.; Masoumi, H.; Ghaemi, A. Experimental, response surface methodology (RSM) and mass transfer modeling of heavy metals elimination using dolomite powder as an economical adsorbent. *Case Stud. Chem. Environ. Eng.* **2023**, *7*, 100329. [CrossRef]
50. Mohrazi, A.; Ghasemi-Fasaei, R.; Mojiri, A.; Safarzadeh, S. Identification of influential parameters and conditions in heavy metals adsorption onto Cal-LDH-PC using optimization approaches of RSM and Taguchi. *Sci. Rep.* **2024**, *14*, 13225. [CrossRef]
51. Boulika, H.; El Hajam, M.; Hajji Nabih, M.; Riffi Karim, I.; Idrissi Kandri, N.; Zerouale, A. Definitive screening design applied to cationic & anionic adsorption dyes on Almond shells activated carbon: Isotherm, kinetic and thermodynamic studies. *Mater. Today Proc.* **2023**, *72*, 3336–3346. [CrossRef]
52. Jokić Govedarica, J.; Tomašević Pilipović, D.; Gvoić, V.; Kerkez, Đ.; Leovac Maćerak, A.; Slijepčević, N.; Bečelić-Tomin, M. Cost-effective method of simultaneous removal of copper and phosphate on environmentally friendly nanomaterial. *J. Serbian Chem. Soc.* **2024**, *89*, 581–595. [CrossRef]
53. Bayuo, J.; Rwiza, M.; Mtei, K. Response surface optimization and modeling in heavy metal removal from wastewater—A critical review. *Environ. Monit. Assess.* **2022**, *194*, 351. [CrossRef]
54. Hayasaka, R.; Hänisch, J.; Cayado, P. DSDApp: An Open-Access Tool for Definitive Screening Design. *J. Open Res. Softw.* **2024**, *12*, 2–8. [CrossRef]
55. Jokić Govedarica, J.; Tomašević Pilipović, D.; Gvoić, V.; Kerkez, Đ.; Leovac Maćerak, A.; Slijepčević, N.; Bečelić-Tomin, M. Eco-friendly nanoparticles: Mechanisms and capacities for efficient removal of heavy metals and phosphate from water using definitive screening design approach. *Environ. Geochem. Health* **2024**, *46*, 118. [CrossRef]
56. Hundie, K.B.; and Akuma, D.A. Optimization of biodiesel production parameters from Prosopisjulifera seed using definitive screening design. *Heliyon* **2022**, *8*, e08965. [CrossRef]
57. Jones, B.; and Nachtsheim, C.J. Definitive screening designs with added two-level categorical factors. *J. Qual. Technol.* **2013**, *45*, 121–129. [CrossRef]
58. El-Sharkawy, R.M.; Khairy, M.; Abbas, M.H.H.; Zaki, M.E.A.; El-Hadary, A.E. Innovative optimization for enhancing $Pb^{2+}$ biosorption from aqueous solutions using Bacillus subtilis. *Front. Microbiol.* **2024**, *15*, 1384639. [CrossRef] [PubMed]
59. Hamdzah, M.; Ujang, Z.; Nasef, M.; Abdullah, N.; Dahalan, F. Removal of Ni(II), Zn(II) and Pb(II) from aqueous solutions using cation-exchange resin in fixed-bed column. *Desalination Water Treat.* **2015**, *57*, 1095118. [CrossRef]
60. Botelho Junior, A.B., Jr.; de Vicente, A.A.; Espinosa, D.C.R.; Tenório, J.A.S. Recovery of metals by ion exchange process using chelating resin and sodium dithionite. *J. Mater. Res. Technol.* **2019**, *8*, 4464–4469. [CrossRef]

61. Monteserin, C.; Blanco, M.; Aranzabe, E.; Aranzabe, A.; Jose, L.; Aitor, L.; Vilas, J. Effects of graphene oxide and chemically-reduced graphene oxide on the dynamic mechanical properties of epoxy amine composites. *Polymers* **2017**, *9*, 449. [CrossRef]
62. Tahereh, K.; Sharif, M.; Pourabas, B. Polythiophene-graphene oxide doped epoxy resin nanocomposites with enhanced electrical, mechanical and thermal properties. *RSC Adv.* **2016**, *6*, 93680–93693. [CrossRef]
63. Bertolucci, E. Chemical and magnetic properties characterization of magnetic nanoparticles. In Proceedings of the IEEE International Instrumentation and Measurement Technology Conference (I2MTC) Proceedings, Pisa, Italy, 11–14 May 2015; pp. 1492–1496. [CrossRef]
64. Nguyen, T.T.; Nguyen Thi, Q.A.; Le, N.H. Synthesis of a novel porous $Ag_2O$ nanomaterial on ion exchange resin and its application for COD determination of high salinity water. *Sci. Rep.* **2021**, *11*, 11487. [CrossRef]
65. Dhumal, J.; Bandgar, S.; Zipare, K.; Shahane, G. $Fe_3O_4$ Ferrofluid Nanoparticles: Synthesis and Rheological Behavior. *Int. J. Mater. Chem. Phys.* **2015**, *1*, 141–145.
66. Munasir, M.; Setyaningsih, S.; Yanasin, S.; Supardi, Z.A.I.; Taufiq, A.; Sunaryono, S. Phase and Magnetic Properties of $Fe_3O_4/SiO_2$ Natural Materials-Based Using Polyethylene Glycol Media. *IOP Conf. Ser. Mater. Sci. Eng.* **2019**, *515*, 012017. [CrossRef]
67. Kristiansen, A.B.; Church, N.; Uçar, Ş. Investigation of magnetite particle characteristics in relation to crystallization pathways. *Powder Technol.* **2023**, *415*, 118145. Available online: https://hdl.handle.net/11511/103007 (accessed on 23 August 2024). [CrossRef]
68. Trakal, L.; Veselská, V.; Šafařík, I.; Vítková, M.; Číhalová, S.; Komárek, M. Lead and cadmium sorption mechanisms on magnetically modified biochars. *Bioresour. Technol.* **2016**, *203*, 318–324. [CrossRef]
69. Raji, Z.; Karim, A.; Karam, A.; Khalloufi, S. Adsorption of Heavy Metals: Mechanisms, Kinetics, and Applications of Various Adsorbents in Wastewater Remediation—A Review. *Waste* **2023**, *1*, 775–805. [CrossRef]
70. Qiu, X.; Hu, H.; Yang, J.; Wang, C.; Cheng, Z. Selective removal of copper from the artificial nickel electrolysis anolyte by a novel chelating resin: Batch, column and mechanisms. *J. Dispers. Sci. Technol.* **2019**, *41*, 137–147. [CrossRef]
71. Zhou, J.; Liu, Y.; Zhou, X.; Ren, J.; Zhong, C. Removal of mercury ions from aqueous solution by thiourea-functionalized magnetic biosorbent: Preparation and mechanism study. *J. Colloid Interface Sci.* **2017**, *507*, 107–118. [CrossRef] [PubMed]
72. Chen, X.; Hossain, F.; Duan, C.; Lu, J.; Tsang, Y.F.; Islam, S.; Zhou, Y. Isotherm models for adsorption of heavy metals from water—A review. *Chemosphere* **2022**, *307*, 135545. [CrossRef]
73. Sari, A.; Tuzen, M.; Citak, D.; Soylak, M. Equilibrium, kinetic and thermodynamic studies of adsorption of Pb(II) from aqueous solution onto Turkish kaolinite clay. *J. Hazard. Mater.* **2007**, *149*, 283–291. [CrossRef]
74. Wang, X.S.; Huang, J.; Hu, H.Q.; Wang, J.; Qin, Y. Determination of kinetic and equilibrium parameters of the batch adsorption of Ni(II) from aqueous solutions by Na-mordenite. *J. Hazard. Mater.* **2007**, *142*, 468–476. [CrossRef]
75. Fadel, D.; El-Bahy, S.; Abdelaziz, Y. Heavy metals removal using iminodiacetate chelating resin by batch and column techniques. *Desalination Water Treat.* **2016**, *57*, 25718–25728. [CrossRef]
76. Nastasović, A.; Marković, B.; Suručić, L.; Onjia, A. Methacrylate-Based Polymeric Sorbents for Recovery of Metals from Aqueous Solutions. *Metals* **2022**, *12*, 814. [CrossRef]
77. Stefan, D.S.; and Meghea, I. Mechanism of simultaneous removal of $Ca^{2+}$, $Ni^{2+}$, $Pb^{2+}$ and $Al^{3+}$ ions from aqueous solutions using Purolite® S930 ion exchange resin. *Comptes Rendus Chim.* **2014**, *17*, 496–502. [CrossRef]
78. Yu, Z.; Qi, T.; Qu, J.; Wang, L.; Chu, J. Removal of Ca(II) and Mg(II) from potassium chromate solution on Amberlite IRC 748 synthetic resin by ion exchange. *J. Hazard. Mater.* **2009**, *167*, 406–412. [CrossRef]
79. Zainol, Z.; and Nicol, M.J. Ion-exchange equilibria of $Ni^{2+}$, $Co^{2+}$, $Mn^{2+}$ and $Mg^{2+}$ with iminodiacetic acid chelating resin Amberlite IRC 748. *Hydrometallurgy* **2009**, *99*, 175–180. [CrossRef]


**Disclaimer/Publisher's Note:** The statements, opinions and data contained in all publications are solely those of the individual author(s) and contributor(s) and not of MDPI and/or the editor(s). MDPI and/or the editor(s) disclaim responsibility for any injury to people or property resulting from any ideas, methods, instructions or products referred to in the content.